Gravitational waveforms from a point particle orbiting a Schwarzschild black hole

Karl Martel
Department of Physics, University of Guelph, Guelph, Ontario, Canada, N1G 2W1
(Received 5 November 2003; published 27 February 2004)

We numerically solve the inhomogeneous Zerilli-Moncrief and Regge-Wheeler equations in the time domain. We obtain the gravitational waveforms produced by a point particle of mass μ traveling around a Schwarzschild black hole of mass M on arbitrary bound and unbound orbits. Fluxes of energy and angular momentum at infinity and the event horizon are also calculated. Results for circular orbits, selected cases of eccentric orbits, and parabolic orbits are presented. The numerical results from the time-domain code indicate that, for all three types of orbital motion, black hole absorption contributes less than 1% of the total flux, so long as the orbital radius $r_p(t)$ satisfies $r_p(t)>5M$ at all times.

DOI: 10.1103/PhysRevD.69.044025 PACS number(s): 04.30.Db, 04.25.Nx, 04.70.−s

I. INTRODUCTION

Tightly bound binary systems consisting of a compact object of a few solar masses and a supermassive black hole of $(10^6–10^9)M_\odot$ are very promising sources of gravitational waves for space-based detectors such as the Laser Interferometer Space Antenna (LISA) [1]. There is now strong evidence that most galaxies harbor a $(10^6–10^9)M_\odot$ supermassive black hole in their center [2], and that they are likely surrounded by a large population of solar-mass compact objects that reside in the galactic cusp [3].

The motion of objects in the galactic cusp is governed by the gravity of the supermassive black hole, but they are also constantly scattered due to the presence of multiple compact objects. For a given compact object, this process occurs until it settles on a highly eccentric orbit that is tightly bound to the central black hole. On such an orbit, the object passes very close to the black hole at periastron and it emits a significant amount of gravitational waves. Capture occurs for those orbits that are sufficiently eccentric and have a sufficiently small periastron (on the order of M) [4]. In these cases, orbital evolution is driven by emission of gravitational waves, and the binary strongly radiates gravitational radiation, until the final plunge of the compact object into the central black hole.

The question is then to determine the rate at which solar-mass compact objects are captured by the central black hole and how quickly the orbits decay by emission of gravitational waves. Because capture occurs when the time to evolve due to emission of gravitational waves is much smaller than the time to evolve due to diffusion and scattering, determination of the type of orbits for which capture occurs and estimate of capture rates are sensitive to the strength of gravitational wave emission. Current estimates of orbital parameters for which capture occurs and associated capture rates are based on the quadrupole approximation for the emission of gravitational waves [5]. Although this is well justified for large periastron, it is not a good approximation for highly eccentric orbits with small periastron, those of interest for gravitational-wave astronomy.

In this paper, we consider a situation in which the compact object has already been captured by a spherically symmetric central black hole, and calculate the correct, general relativistic, rates at which the system loses energy and angular momentum to gravitational waves. We consider three types of orbits: circular, eccentric, and parabolic orbits. These calculations will then be used to refine capture rate estimates, but this will be left for future work.

At this level of approximation, the internal dynamics of the small compact object are irrelevant. We treat it as a point particle and base our calculations on first-order perturbations of a Schwarzschild black hole; this is appropriate in view of the small mass ratio involved. The gravitational waveforms produced by the orbital motion are obtained by solving the even parity Zerilli-Moncrief [6,7] (ZM) and the odd parity Regge-Wheeler [8] (RW) equations. We work with Schwarzschild coordinates, for which both wave equations take the form

$$\left[-\frac{\partial^2}{\partial t^2}+\frac{\partial^2}{\partial r^{*2}}-V_l(r)\right]\psi_{lm}(r,t)=S_{lm}(r,t), \qquad (1.1)$$

where $r^*=r+2M\log(r/2M-1)$ is the usual tortoise coordinate, and $V_l(r)$ is a potential defined in Eq. (A4) for both modes. Explicit definitions for the ZM and the RW functions are given in Eqs. (A2) and (A3) of Appendix A. The source term $S_{lm}(r,t)$ is of the form

$$S_{lm}(r,t)=G(r,t)\,\delta[r-r_p(t)]+F(r,t)\,\delta'[r-r_p(t)], \qquad (1.2)$$

where a prime denotes an r derivative, $r_p(t)$ denotes the radial position of the particle as a function of time, and $G(r,t)$ and $F(r,t)$ are known functions of r and t once the orbital motion of the particle is specified; they are given by Eq. (A6) for the Zerilli-Moncrief equation, and by Eq. (A7) for the Regge-Wheeler equation.

Instead of Fourier decomposing Eq. (1.1) and solving in the frequency domain, we choose to integrate them in the time domain. The numerical method we use was first developed by Lousto and Price [9], and later corrected by Martel and Poisson to yield second-order convergence [10]; it is a finite-difference scheme, based on the null cones of the Schwarzschild spacetime, which incorporates the source term without approximating $\delta[r-r_p(t)]$ and $\delta'[r-r_p(t)]$. This method is advantageous compared to Fourier decompo-

sition because of the need, in the case of highly eccentric orbits, to sum over a very large number of frequencies in order to obtain accurate results [11,12]. As an added bonus, the time-domain method provides the Zerilli-Moncrief and Regge-Wheeler functions everywhere in the spacetime. For each multipole moment, information about the fluxes of energy and angular momentum at infinity and through the event horizon is obtained by a single numerical integration.

Astrophysical black holes are very likely to be rapidly rotating and the assumption of spherical symmetry for the central black hole is unrealistic. However, removing this assumption would require a substantial revision of our numerical method. The source term for the Schwarzschild perturbation equations can be treated exactly because, by removing the angular dependence, the problem is reduced to integrating a one-dimensional partial differential equation. A divergent source term of the form of Eq. (1.2) then leads to a simple jump in the field at the particle's position, and this can easily be handled by finite-difference methods. For a rotating black hole, one is faced with the task of solving the inhomogeneous Teukolsky equation [13]. It is well known that this equation is not separable in the time domain, because the eigenvalues of the angular functions are frequency dependent. Insisting on working in the time domain leaves a two-dimensional partial differential equation to integrate. Unfortunately, a δ-function source no longer leads to a simple jump at the position of the particle: the field is now (logarithmically) divergent at this location. Standard finite-difference methods are inadequate to deal with this type of behavior and cannot be used. The problem can be circumvented by smearing the particle around its position (for example by using narrow Gaussian functions instead of δ functions). This eliminates the divergence in the source term and, consequently, in the field; standard finite-difference methods can then be applied. Such an approach has been used to obtain gravitational waveforms produced by a particle on an equatorial circular orbit of the Kerr black hole [14], but the error introduced by smearing the particle is difficult to ascertain. By specializing to Schwarzschild, comparison with the present work will allow such a determination; this is another important justification for the work presented here. With this application in mind, we consider orbits with a wide range of eccentricities and semi-major axis, and do not necessarily restrict ourselves to highly eccentric orbits.

The paper is organized as follows. In Sec. II we describe the orbital parametrization of bound and marginally bound geodesics of the Schwarzschild spacetime. In Sec. III A we provide a relation between the Zerilli-Moncrief and Regge-Wheeler functions and the gravitational waveforms at infinity and near the event horizon; from these relations, the fluxes of energy and angular momentum can be calculated. In Sec. III B, we provide a discussion of numerical issues that limit the accuracy with which we can determine the fluxes. In Sec. III C, Sec. III D, and Sec. III E, we present our results for the gravitational waveforms and fluxes for circular, eccentric, and parabolic orbits, respectively. In Sec. IV, we summarize our findings. Appendix A contains a brief summary of first-order black hole perturbation theory, while Appendix B contains a detailed derivation of the flux formulas at infinity (Appendix B 3) and through the event horizon (Appendix B 4).

II. ORBITAL PARAMETRIZATION

Following Cutler *et al.* [12], we introduce p, the semi-latus rectum, and e, the eccentricity, as orbital parameters. They are defined so that the periastron and apastron are at $pM/(1+e)$ and $pM/(1-e)$, respectively. In terms of these parameters, the energy and angular momentum per unit mass of a point particle are

$$\tilde{E}^2=\frac{(p-2-2e)(p-2+2e)}{p(p-3-e^2)},$$

$$\tilde{L}^2=\frac{M^2p^2}{p-3-e^2}. \tag{2.1}$$

For $e=0$ the periastron and apastron coincide, and the orbit is circular. In the interval $0\leqslant e<1$, the motion occurs between two turning points, while for $e=1$, the apastron is pushed back to infinity and the motion is parabolic.[1] In all cases, stable orbits exist only if $p>6+2e$.

The position of the particle at time t is given by the coordinates $(r_p(t),\varphi_p(t),\theta_p=\pi/2)$. Inspired by the solution to the two-body problem in Newtonian mechanics, the radial position of the particle is expressed as

$$r_p(\chi)=\frac{pM}{1+e\cos\chi}, \tag{2.2}$$

where χ is a parameter along the orbit. This is well behaved at the turning points ($\chi=0,\ \pi$), which facilitates the numerical integration of the geodesic equations for the time and angular coordinates. In terms of χ, these are [12]

[1]In analogy with Newtonian mechanics, we use the term "parabolic" for marginally bound orbits: they have $e=1$ ($\tilde{E}=1$), but the trajectories traced out are *not* parabolas, except in the limit $p\gg 1$.

$$\frac{d}{d\chi}t=Mp^2\frac{(p-2-2e)^{1/2}(p-2+2e)^{1/2}}{(p-2-2e\cos\chi)(1+e\cos\chi)^2(p-6-2e\cos\chi)^{1/2}}, \tag{2.3}$$

$$\frac{d}{d\chi}\varphi_p=\frac{p^{1/2}}{(p-6-2e\cos\chi)^{1/2}}. \tag{2.4}$$

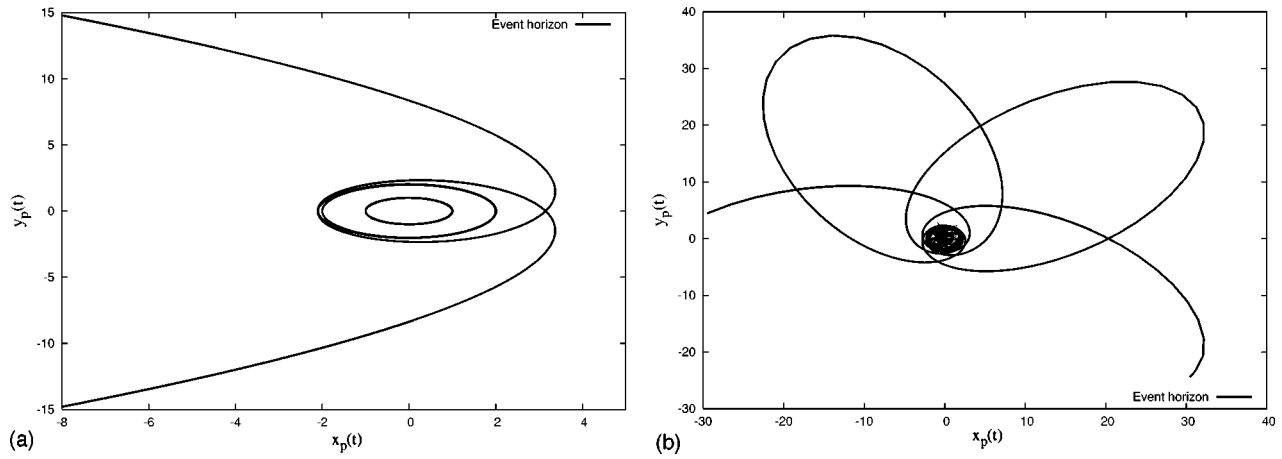

FIG. 1. In the left panel, we display the trajectories in the x_p-y_p plane for a geodesic with $e=1$, and $p=8.001$. For this choice of parameters, the particle orbits the black hole approximately four times before leaving the central region. In the right panel, we display a $e=0.9$ and $p=7.8001$ geodesic. When the particle reaches the periastron, it orbits the black hole on a quasi-circular orbit for approximately six cycles. In both cases, the exact number of cycles is given by Eq. (2.5).

The first of these equation can be numerically inverted to yield $\chi(t)$; knowledge of $r_p(\chi)$ and $\varphi_p(\chi)$ is then equivalent to knowing $r_p(t)$ and $\varphi_p(t)$.

The geodesic equations given by Eqs. (2.3) and (2.4) are integrated using the Burlisch-Stoer method [15], and we chose the initial conditions as follows. The gravitational waveforms are extracted as functions of time at a location r^*_{obs}. We take the initial moment $t=-t_o<0$ to be the one at which the particle is at periastron [$\chi=0$, $r_p(-t_o)=Mp/(1+e)$, and $\varphi_p(-t_o)=0$]. We set t_o equal to the light travel time between the periastron and the observation point. Thus, radiation emitted at the initial moment will reach the observer at $t\approx 0$.

This parametrization of the geodesic is suitable for bound and unbound orbits of the Schwarzschild spacetime; for $e<1$, the parameter χ can take any real value, whereas for $e\geqslant 1$, it is confined to $-\pi/e\leqslant\chi\leqslant\pi/e$. In this paper, we consider circular orbits, selected cases of eccentric orbits, and parabolic orbits ($e=1$), but the code is capable of producing gravitational waveforms for any value of e. For any p and e, the particle orbits the central black hole a number $N=\Delta\varphi_p/(2\pi)$ of times before moving out of the central region. Integrating Eq. (2.4) over one radial period yields [12]

$$N=\frac{2}{\pi}\sqrt{\frac{p}{p-6+2e}}K\left(\frac{4e}{p-6+2e}\right), \tag{2.5}$$

where $K(m)=\int_0^{\pi/2}dx(1-m\sin^2 x)^{-1/2}$ is the complete elliptic integral of the first kind. To visualize the trajectories, we introduce $x_p(t)=r_p(t)/(2M)\cos[\varphi_p(t)]$ and $y_p(t)=r_p(t)/(2M)\sin[\varphi_p(t)]$. In Fig. 1, we display trajectories in the x_p-y_p plane for $p=7.8001$ and $e=0.9$ (left), and $p=8.001$ and $e=1$ (right). In both cases, the number of times the particle orbits the central black hole is large. This is because p is close to the critical value $6+2e$ at which N diverges. In these cases, gravitational-wave emission is dominated by the quasi-circular portion of the orbit near periastron. The total energy emitted is then well approximated by $E=NE_{circular}$, where N is the (divergent) number of orbits, P the period of a circular orbit at $r_p=Mp/(1+e)$, and $E_{circular}$ the energy emitted by a particle on such an orbit; a similar approximation holds for L.

III. WAVEFORMS, ENERGY AND ANGULAR MOMENTUM RADIATED

To numerically evolve Eq. (1.1) initial conditions must be provided for the gravitational perturbations. The manner in which the initial configuration of the gravitational field influences the subsequent evolution has been studied previously for radial geodesics [10]. For bound geodesics, the motion is quasi-periodic and waiting a sufficiently long time eliminates the contribution from the initial conditions, which simply propagates away. For marginally bound geodesics, we chose the initial position of the particle to be very far from the periastron. Far away from the black hole, the velocity of the particle is small and it takes much longer for the particle to reach periastron than for the initial gravitational-wave content to escape from the system. At the point where the emission of radiation is strongest, there is no trace left of the initial configuration of the gravitational perturbations. This allows us to completely avoid problems related to the choice of initial data for both bound and marginally bound geodesics. We chose zero initial conditions for the gravitational perturbations, acknowledging that this is inconsistent (creating the particle from nothing violates energy-momentum conservation), but recognizing that artifacts of this choice disappear in time. Fluxes may then be computed reliably after waiting a sufficiently long time.

A. Far-zone fluxes and black hole absorption

We first provide a short summary of the relations between the Zerilli-Moncrief and the Regge-Wheeler functions and the radiative portion of the metric perturbation at infinity and

at the event horizon, as well as flux formulas used throughout the paper. Complete summaries of first-order black hole perturbation theory and flux calculations are relegated to Appendixes A and B, respectively. In the radiation zone, the two gravitational-wave polarizations are related to the Zerilli-Moncrief and the Regge-Wheeler functions by

$$h_+ - \imath h_\times = \frac{1}{2r}\sum_{lm}\sqrt{\frac{(l+2)!}{(l-2)!}} \times\left(\psi_{ZM}(t) - 2\imath\int^t dt'\,\psi_{RW}(t')\right){}_{-2}Y^{lm}(\theta,\varphi). \tag{3.1}$$

Similarly, when $r\to 2M$, the two gravitational-wave polarizations are given by

$$h_+ + \imath h_\times = \frac{1}{4M}\sum_{lm}\sqrt{\frac{(l+2)!}{(l-2)!}} \times\left(\psi_{ZM}(t) - 2\imath\int^t dt'\,\psi_{RW}(t')\right){}_{2}Y^{lm}(\theta,\varphi). \tag{3.2}$$

In these equations, ${}_sY^{lm}$ are spherical harmonics of spin weight s [16].

From Isaacson's stress-energy tensor for gravitational waves [17], as well as Eqs. (3.1) and (3.2), we calculate the energy flux in each multipole moment to be

$$\dot{E}^{\infty,eh}_{lm} = \begin{cases} \dfrac{1}{64\pi}\dfrac{(l+2)!}{(l-2)!}|\dot{\psi}_{ZM}|^2, & l+m \ \text{even}, \\ \dfrac{1}{16\pi}\dfrac{(l+2)!}{(l-2)!}|\psi_{RW}|^2, & l+m \ \text{odd}, \end{cases} \tag{3.3}$$

and the angular momentum flux to be

$$\dot{L}^{\infty,eh}_{lm} = \begin{cases} \dfrac{\imath m}{128\pi}\dfrac{(l+2)!}{(l-2)!}\dot{\psi}_{ZM}\tilde{\psi}_{ZM} + \text{c.c.}, & l+m \ \text{even}, \\ \dfrac{\imath m}{32\pi}\dfrac{(l+2)!}{(l-2)!}\psi_{RW}\displaystyle\int dt\,\tilde{\psi}_{RW} + \text{c.c.}, & l+m \ \text{odd}, \end{cases} \tag{3.4}$$

where a tilde over a quantity denotes complex conjugation, c.c. is the complex conjugate, and the l and m indices are implicit on ψ_{ZM} and ψ_{RW}. In Eqs. (3.3) and (3.4), $\dot{E}^{\infty}_{lm}$ and $\dot{L}^{\infty}_{lm}$ denote the fluxes across a surface $r=\text{const}\to\infty$, while $\dot{E}^{eh}_{lm}$ and $\dot{L}^{eh}_{lm}$ denote the fluxes through a surface $r=\text{const}\to 2M$. The fluxes at infinity are calculated using the Zerilli-Moncrief and Regge-Wheeler functions extracted at $r^*=r^*_{obs}$, where r^*_{obs} is large and positive, while for the horizon fluxes, they are extracted at $r^*=r^*_{eh}$, where r^*_{eh} is large and negative. Once $\dot{E}_{lm}$ and $\dot{L}_{lm}$ are known, the total fluxes are obtained by summing over all modes:

$$\dot{E}^{\infty,eh} = \sum_{l=2}^{\infty}\dot{E}^{\infty,eh}_{l}, \quad \dot{E}^{\infty,eh}_{l} = \dot{E}^{\infty,eh}_{l0} + 2\sum_{m=1}^{l}\dot{E}^{\infty,eh}_{lm}, \tag{3.5}$$

$$\dot{L}^{\infty,eh} = \sum_{l=2}^{\infty}\dot{L}^{\infty,eh}_{l}, \ \text{and} \quad \dot{L}^{\infty,eh}_{l} = 2\sum_{m=1}^{l}\dot{L}^{\infty,eh}_{lm}; \tag{3.6}$$

there is no $m=0$ contribution to the angular momentum flux, and the factor of 2 in front of $\dot{E}^{\infty,eh}_{lm}$ and $\dot{L}^{\infty,eh}_{lm}$ comes from folding the $m<0$ contributions over to $m>0$ (see Appendix A). In a slow-motion, weak-field approximation the quadrupole moment dominates ($l=2$ and $m=2$) and the total energy and angular momentum radiated over one orbital period are [18]

$$E_Q(p,e) = \frac{64\pi}{5}\frac{\mu^2}{M}\left(1+\frac{73}{24}e^2+\frac{37}{96}e^4\right)p^{-7/2}, \tag{3.7}$$

$$L_Q(p,e) = \frac{64\pi}{5}\mu^2\left(1+\frac{7}{8}e^2\right)p^{-2}. \tag{3.8}$$

The average energy and angular momentum radiated per unit time, defined by performing an orbital average, are

$$\langle\dot{E}_Q\rangle = \frac{32}{5}\left(\frac{\mu}{M}\right)^2\frac{(1-e^2)^{3/2}}{p^5}\left(1+\frac{73}{24}e^2+\frac{37}{96}e^4\right),$$

$$\langle\dot{L}_Q\rangle = \frac{32}{5}\frac{\mu^2}{M}\frac{(1-e^2)^{3/2}}{p^{7/2}}\left(1+\frac{7}{8}e^2\right). \tag{3.9}$$

For the binaries considered in this paper, the slow-motion and weak-field approximations break down, and the fluxes must be computed using Eqs. (3.5) and (3.6). Numerically we cannot perform the infinite sums, and we truncate them at a finite value l_{max}. In the next subsection, we explain the criteria used to choose l_{max} and discuss the overall accuracy of the time-domain computation.

B. Accurate determination of the fluxes: Numerical issues

In order to calculate the fluxes to a relative accuracy ε (we use $\varepsilon=0.01$), we need to consider three sources of error: discretization of Eq. (1.1), effects of the finite size of our computational grid, as well as truncation of the sums in Eqs. (3.5) and (3.6).

First, discretization of Eq. (1.1) introduces numerical truncation errors. In a previous paper, we showed that the Lousto and Price algorithm can be corrected to yield second-order convergence [10], i.e. truncation errors scale as Δt^2, with Δt denoting the numerical step size for evolution. Throughout this work we generated gravitational waveforms by setting $\Delta t = 0.1(2M)$ in the numerical algorithm; this proved sufficient to determine the fluxes at infinity to the desired 1% accuracy. However, for a given step size the fluxes through the event horizon are never determined as accurately as the fluxes at infinity. The gravitational waves flowing through the event horizon are weaker than the ones

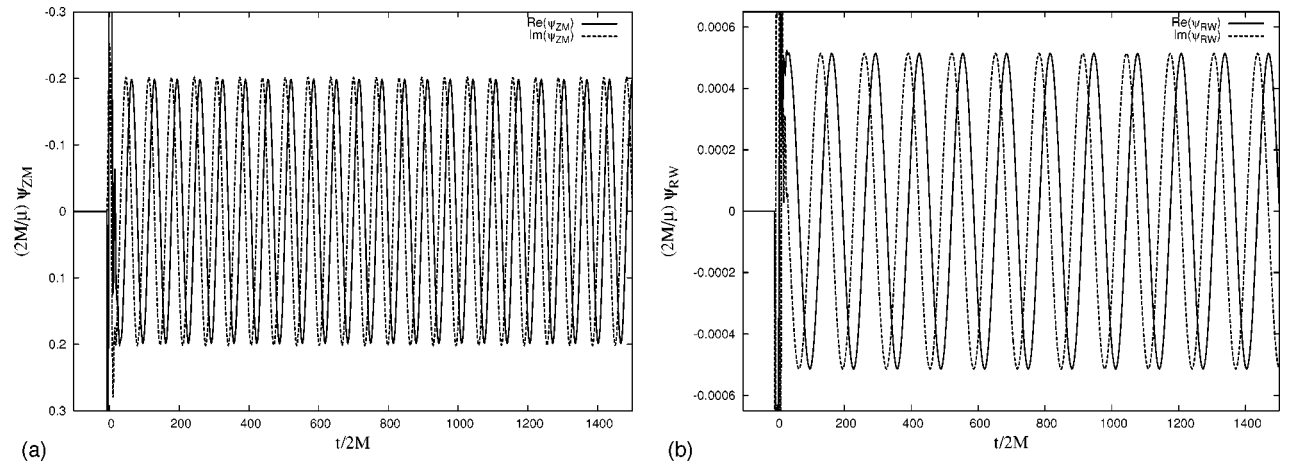

FIG. 2. The dominant radiation modes for the Zerilli-Moncrief (left, $l=2$ and $m=2$) and Regge-Wheeler (right, $l=2$ and $m=1$) functions for a particle orbiting the black hole at $r_p=12M$. At early times, the waveforms are dominated by the initial data content. We calculate the energy and angular momentum fluxes after a time $t/(2M)=350.0$.

escaping to infinity, and, because of this difference in scales, horizon fluxes are determined with an accuracy $\lesssim 5\%$. But we will see below that horizon fluxes *never* amount to more than a few percent of the total fluxes. The lower accuracy with which black hole absorption is determined is then sufficient for our goal of 1% overall accuracy.

Second, the expressions for the fluxes displayed in Eqs. (3.3) and (3.4) hold only asymptotically ($r^*\to\pm\infty$). Numerically we are forced to extract the waveforms at finite r^* values, and this introduces finite-size effects in our results. Numerical efficiency requires a small computational grid, but accuracy requires the waveforms to be extracted at a large and positive r^*_{obs} and at a large and negative r^*_{eh}. The flux formulas developed here are based on the stress-energy tensor for gravitational waves, as constructed by Isaacson [17]. The validity of the construction depends on $\lambda/\mathcal{R}\ll 1$ being satisfied, where λ is a wavelength of the radiation and $\mathcal{R}$ a typical radius of curvature. To calculate the fluxes far from the black hole, we extract the waveforms in an approximate radiation zone defined by $\lambda/r_{obs}\ll 1$, where $\lambda^{-1}\sim(M/R_p^3)^{1/2}$ and R_p is a typical orbital radius. The radiation zone is then defined by $R_p/r_{obs}(R_p/M)^{1/2}\ll 1$. For relativistic motion $R_p\sim M$ and by imposing $R_p/r_{obs}<\varepsilon$, we make an error of order ε in approximating the radiation zone. This is somewhat different from the criteria for the validity of Isaacson's stress-energy tensor, but since $\mathcal{R}^{-1}\sim(M/r_{obs}^3)^{1/2}$, we have that $\lambda/\mathcal{R}\sim(R_p/r_{obs})^{3/2}\sim\varepsilon^{3/2}$, and the use of the stress-energy tensor is justified. In practice we also imposed $r^*_{obs}>750(2M)$. At the horizon, the situation is somewhat different. The typical radius of curvature is $\mathcal{R}\sim\sqrt{2}2M$, but the radiation is blueshifted so that $\lambda\sim f_{eh}(R_p^3/M)^{1/2}\to 0$, where $f_{eh}=1-2M/r_{eh}$. The requirement $\lambda/\mathcal{R}\ll 1$ then translates to $f_{eh}[R_p/(2M)]^{3/2}<\varepsilon$. We used $R^*_p/|r^*_{eh}|<\varepsilon$, as well as $r^*_{eh}<-750(2M)$, which amply satisfies the above requirement. This yielded good results, but a better, more efficient choice would have been $r_{eh}=2M[1+(2M/R_p)^{3/2}\varepsilon]$. With these choices of r^*_{obs} and r^*_{eh}, we are making an error of *at most* order ε in determining the fluxes at infinity and through the event horizon, respectively.

Finally, the last source of error limiting the accuracy of the determination of the fluxes arises from truncating the sums in Eqs. (3.5) and (3.6) at a finite value l_{max}. The error is made small enough for our requirements by demanding that

$$\varepsilon\equiv\max\left(\frac{\dot{E}^{\infty}_{l_{max}}}{\dot{E}^{\infty}},\frac{\dot{L}^{\infty}_{l_{max}}}{\dot{L}^{\infty}}\right)\leqslant 1\% \tag{3.10}$$

be satisfied. Typically, Eq. (3.10) is satisfied with l_{max} given by $[p/(1+e)]^{-(l_{max}-2)}<\varepsilon$, which is known to hold for circular orbits [19]. Note that because $\dot{E}^{\infty}_{l_{max}}$ and $\dot{L}^{\infty}_{l_{max}}$ are included in the sum, the error comes from neglecting terms starting at $l=l_{max}+1$. In effect, the relative error made from neglecting these terms is much smaller than 1%. In the following, we will return with empirical estimates of our numerical errors; these will confirm the preceding qualitative discussion.

C. Circular orbits

For circular orbits, $e=0$ and the radius of the orbit is $r_p=pM$. In Fig. 2 we display typical gravitational waveforms emitted by a particle traveling on a circular orbit. Both waveforms have the same pattern: The field oscillates with an angular frequency given by $m\Omega$, where $\Omega=M^{-1}p^{-3/2}$ is the orbital angular velocity and m is the multipole index. The left panel contains the dominant quadrupolar mode ($l=2$ and $m=2$), while the right panel contains the dominant odd parity mode ($l=2$ and $m=1$).

The code outputs $\dot{E}_{GR}$ and $\dot{L}_{GR}$ directly, but it proves convenient to express the fluxes in terms of c_E and c_L: coefficients that remain close to 1 for all values of p. The total fluxes are calculated using Eqs. (3.5) and (3.6) and we express the numerically obtained results in the form

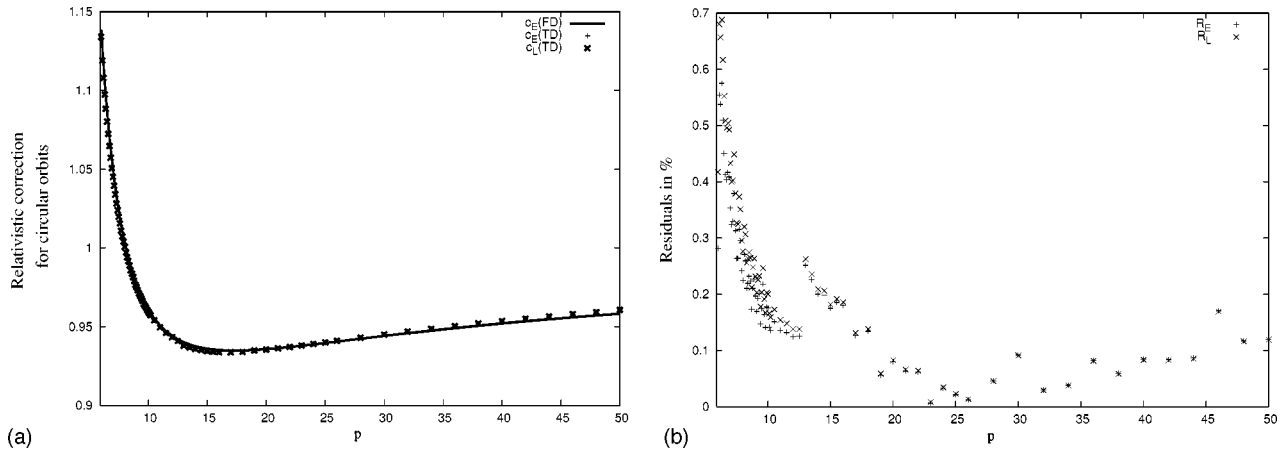

FIG. 3. In the left panel, we display $c_E(FD)$, as well as $c_E(TD)$ and $c_L(TD)$, as functions of p. Both c_E and c_L slowly approach 1 from below for large p. For small values of p, the coefficients approach 1.15 as p approaches 6. In the right panel, we display the residuals R_E and R_L as defined in the text. Using the time-domain method, the fluxes are calculated accurately to 0.7% for $p=6.0001$, and to 0.2% for large values of p.

TABLE I. Energy and angular momentum fluxes for circular orbits, calculated using a time domain (TD) code, are compared with fluxes calculated by Poisson using a frequency domain (FD) approach [20]. Here we chose $p=7.9456$ and $p=46.062$. The energy fluxes are in units of $(M/\mu)^2$, and the angular momentum fluxes are in units of M/μ^2. They are calculated at $r^*_{obs}=1500M$ and $r^*_{obs}=5200M$ for $p=7.9456$ and $p=46.062$, respectively.

l	m	$\dot{E}^\infty$ (FD)	$\dot{E}^\infty$ (TD)	Relative difference	$\dot{L}^\infty$ (FD)	$\dot{L}^\infty$ (TD)	Relative difference
	$p=7.9456$						
2	1	8.1633×10^{-7}	8.1623×10^{-7}	$<0.1\%$	1.8283×10^{-5}	1.8270×10^{-5}	0.1%
	2	1.7063×10^{-4}	1.7051×10^{-4}	$<0.1\%$	3.8215×10^{-3}	3.8164×10^{-3}	0.1%
3	1	2.1731×10^{-9}	2.1741×10^{-9}	$<0.1\%$	4.8670×10^{-8}	4.8684×10^{-8}	$<0.1\%$
	2	2.5199×10^{-7}	2.5164×10^{-7}	0.1%	5.6439×10^{-6}	5.6262×10^{-6}	0.3%
	3	2.5471×10^{-5}	2.5432×10^{-5}	0.1%	5.7048×10^{-4}	5.6878×10^{-4}	0.3%
4	1	8.3956×10^{-13}	8.3507×10^{-13}	0.2%	1.8803×10^{-11}	1.8692×10^{-11}	0.6%
	2	2.5091×10^{-9}	2.4986×10^{-9}	0.4%	5.6195×10^{-8}	5.5926×10^{-8}	0.5%
	3	5.7751×10^{-8}	5.7464×10^{-8}	0.5%	1.2934×10^{-6}	1.2933×10^{-6}	$<0.1\%$
	4	4.7256×10^{-6}	4.7080×10^{-6}	0.4%	1.0584×10^{-4}	1.0518×10^{-4}	0.6%
5	1	1.2594×10^{-15}	1.2544×10^{-15}	0.4%	2.8206×10^{-14}	2.8090×10^{-14}	0.4%
	2	2.7896×10^{-12}	2.7587×10^{-12}	1.1%	6.2479×10^{-11}	6.1679×10^{-11}	1.3%
	3	1.0933×10^{-9}	1.0830×10^{-9}	1.0%	2.4486×10^{-8}	2.4227×10^{-8}	1.1%
	4	1.2324×10^{-8}	1.2193×10^{-8}	1.1%	2.7603×10^{-7}	2.7114×10^{-7}	1.8%
	5	9.4563×10^{-7}	9.3835×10^{-7}	0.8%	2.1179×10^{-5}	2.0933×10^{-5}	1.2%
	Total	2.0317×10^{-4}	2.0273×10^{-4}	0.2%	4.5446×10^{-3}	4.5399×10^{-3}	0.1%
	$p=46.062$						
2	1	1.8490×10^{-11}	1.8713×10^{-11}	1.2%	5.7804×10^{-9}	5.8497×10^{-9}	1.2%
	2	2.8650×10^{-8}	2.8728×10^{-8}	0.3%	8.9566×10^{-6}	8.9809×10^{-6}	0.3%
3	1	7.5485×10^{-14}	7.7275×10^{-14}	2.4%	2.3598×10^{-11}	2.4158×10^{-11}	2.4%
	2	1.0926×10^{-12}	1.0990×10^{-12}	0.6%	3.4157×10^{-10}	3.4359×10^{-10}	0.6%
	3	8.0640×10^{-10}	8.0835×10^{-10}	0.2%	2.5210×10^{-7}	2.5270×10^{-7}	0.2%
4	1	9.9792×10^{-19}	1.0390×10^{-18}	4.1%	3.1191×10^{-16}	3.2480×10^{-16}	4.1%
	2	1.6018×10^{-14}	1.6171×10^{-14}	1.0%	5.0075×10^{-12}	5.0555×10^{-12}	1.0%
	3	4.6603×10^{-14}	4.6799×10^{-14}	0.4%	1.4569×10^{-11}	1.4631×10^{-11}	0.4%
	4	2.7937×10^{-11}	2.7997×10^{-11}	0.2%	8.7339×10^{-9}	8.7525×10^{-9}	0.2%
	Total	2.9505×10^{-4}	2.9584×10^{-8}	0.3%	9.2239×10^{-6}	9.2486×10^{-6}	0.3%

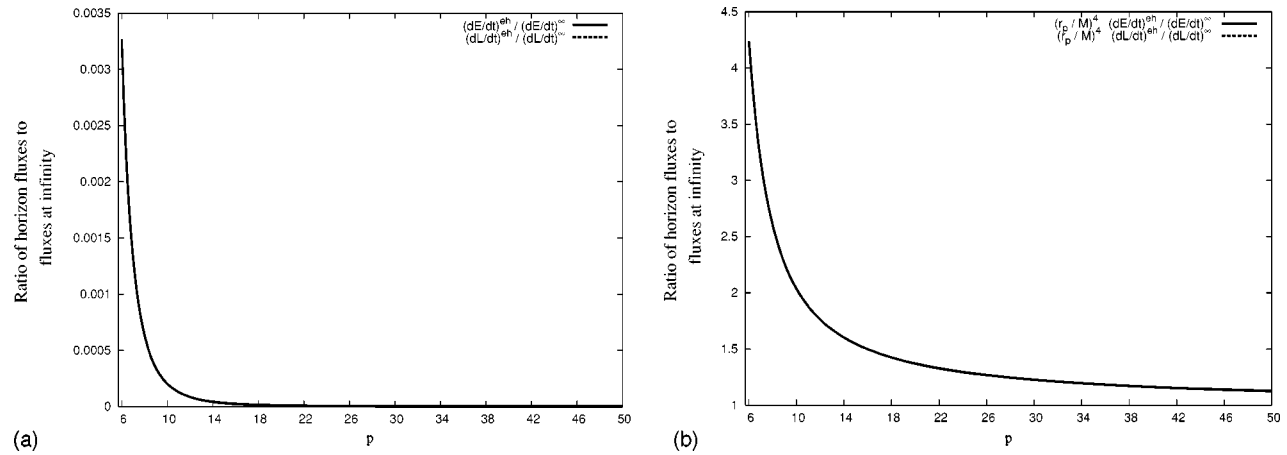

FIG. 4. We display the energy and angular momentum fluxes through the event horizon normalized by the fluxes in the radiation zone. Even for highly relativistic motion, the horizon fluxes contribute less than 0.4% of the total fluxes. For circular orbits, the theoretical prediction is that $\dot{E}^{eh}/\dot{E}^{\infty}=\dot{L}^{eh}/\dot{L}^{\infty}$. Numerically, this relation is only approximate, but nevertheless the two curves are indistinguishable. The right panel displays these ratios normalized by $(r_p/M)^{-4}$, the weak-field and slow-motion approximation.

$$\dot{E}^{\infty}_{GR}(p)=c_E\dot{E}_Q(p,0),$$

$$\dot{L}^{\infty}_{GR}(p)=c_L\dot{L}_Q(p,0), \tag{3.11}$$

where $\dot{E}_Q(p,e)$ and $\dot{L}_Q(p,e)$ are given by Eq. (3.9) above with $e=0$. For circular orbits, we should find $\dot{E}=\Omega\dot{L}$ and therefore, $c_E=c_L$.

Circular orbits have been studied extensively and we use them to quantitatively test the accuracy of the time-domain method. We perform a comparison of our results with the time-domain (TD) code with results obtained in the frequency domain (FD) by Poisson [20]. In the left panel of Fig. 3 we display $c_E(TD)$, $c_L(TD)$, and $c_E(FD)$. In the right panel, we display the residuals, $R_E=100|c_E(TD)-c_E(FD)|/c_E(FD)$ and $R_L=100|c_L(TD)-c_E(FD)|/c_E(FD)$. In the interval $6<p\leqslant 50$, the time-domain code reproduces the frequency domain calculations to 0.7% or better, with the best agreement occurring for large values of p.

In Table I we perform a mode by mode comparison between the two methods for $p=7.9456$ and $p=46.062$. For $p=7.9456$, the fluxes from each multipole moment calculated with the time-domain code agree to 1% or better with the fluxes calculated in the frequency domain. A similar agreement is found for $p=46.062$, with the exception of the $l=3$ and $m=1$, and $l=4$ and $m=1$ modes, for which the relative difference is 2.4% and 4.1%, respectively. This results from the huge difference in amplitude between these modes and the dominant mode. The step size used throughout this work is sufficient to obtain an overall relative accuracy of 1%, but it is not small enough to determine individual, small-amplitude modes to better than 2–5 %. Although these modes could be resolved properly by using a smaller step size, it is not necessary for our goal of 1% overall accuracy; the contributions from these modes to the total fluxes are six and ten orders of magnitude smaller than the leading-order contributions, respectively. As such, they do not affect the overall accuracy of the computation; for $p=7.9456$ and $p=46.062$ the total fluxes calculated with the

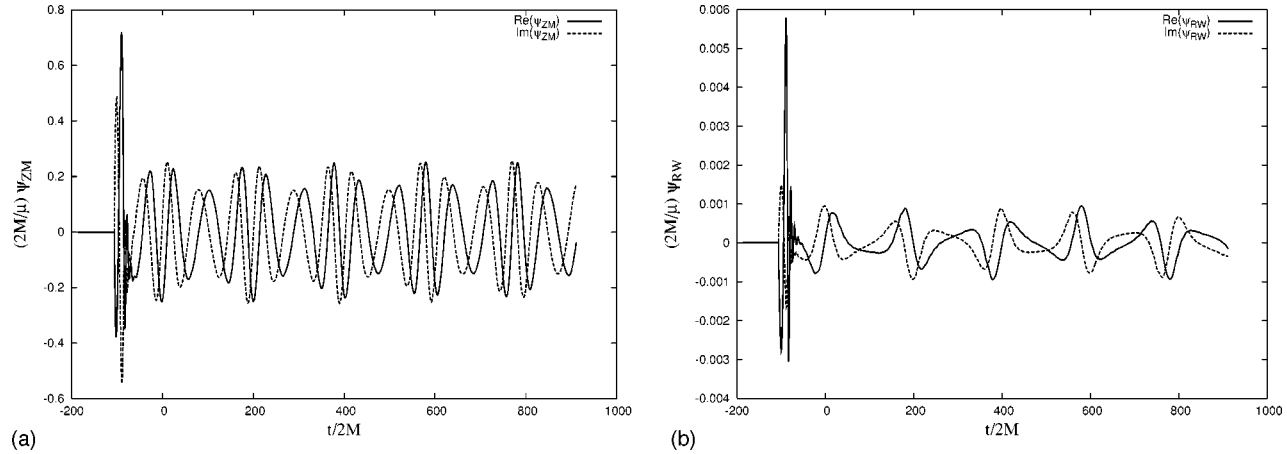

FIG. 5. The Zerilli-Moncrief (left, $l=2,m=2$) and Regge-Wheeler (right, $l=2,m=1$) functions for $p=12$ and $e=0.2$. As in the case of circular orbits, early times are dominated by the initial data content.

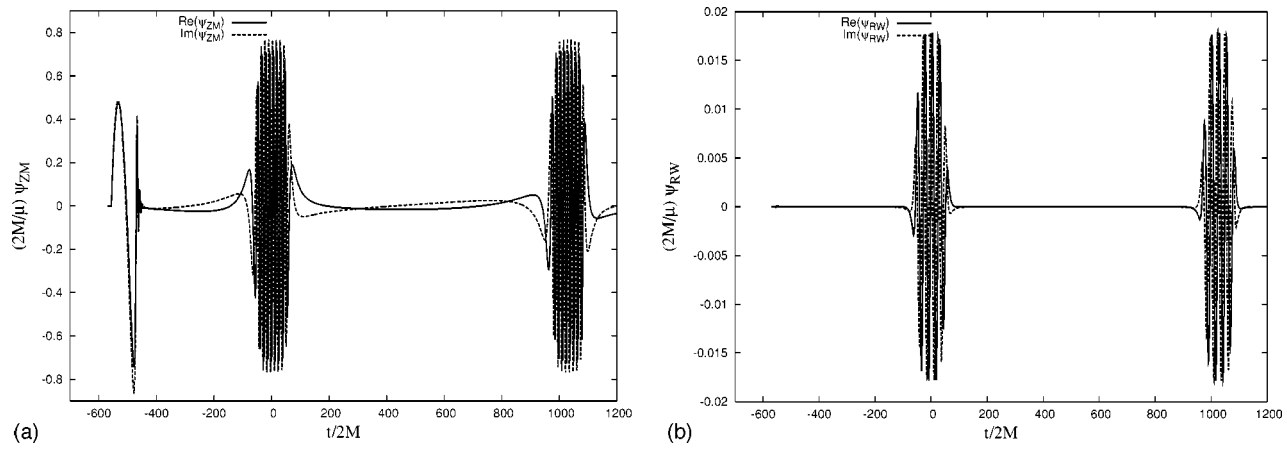

FIG. 6. The Zerilli-Moncrief (left, $l=2,m=2$) and Regge-Wheeler (right, $l=2,m=1$) functions for $p=7.801$ and $e=0.9$. As in the case of circular orbits, early times are dominated by the initial data content. The radiation occurs in short bursts when the particle approaches the periastron. This is typical of the zoom-whirl behavior studied in [11].

time-domain method agree with the frequency domain results to within 0.2% and 0.3%, respectively.

Black hole absorption was calculated in a weak-field and slow-motion approximation for a particle in circular orbit by Poisson and Sasaki [21] and Alvi [22] who showed that it gives rise to a v^8 correction to the quadrupole formula: $\dot{E}^{eh}/\dot{E}_Q = v^8 = \dot{L}^{eh}/\dot{L}_Q$, where $v=p^{-1/2}=(M/r_p)^{1/2}$ is the orbital velocity. The time-domain method allows black hole absorption to be calculated for arbitrary geodesics. In particular, for circular orbits our results show that even when $v\sim 0.4$ and the particle travels in a region of strong gravitational field, the amount of energy and angular momentum absorbed by the black hole is always a small correction to the total fluxes. For highly relativistic motion, this never grows large enough to contribute more than 0.4% of the total fluxes (see left panel of Fig. 4). For the purpose of calculating total fluxes with an overall accuracy of 1%, black hole absorption can safely be ignored. The right panel displays the ratio of horizon fluxes to the fluxes at infinity, normalized by $(M/r_p)^4$, the weak-field and slow-motion approximation. As expected for circular motion, the normalized ratios for energy and angular momentum are equal to each other, and they approach 1 for large p.

We estimate the accuracy with which black hole absorption can be determined using the time-domain method to be 5%. This estimate is based on the following argument. For small amplitude modes, the accuracy with which their contribution to the total fluxes can be determined is limited by errors originating from the discretization of Eq. (1.1) and the finite stepsize used in the numerical evolution. Based on the accuracy of the $l=4$ and $m=1$ mode for $p=46.062$ in Table I, the error is seen to be $\lesssim 5\%$ for modes whose contribution is ten orders of magnitude smaller than the dominant mode. For the range of p values considered in this paper, black hole absorption is at most seven orders of magnitude smaller than the dominant contribution. [This is evaluated using the $(M/r_p)^4$ relation at $r_p=50M$, the value at which black hole absorption is least significant.] It is then safe to assume that fluxes through the event horizon are determined with an accuracy $<5\%$. (For values of p close to $6+2e$, black hole absorption is more important and therefore more accurately determined.)

D. Eccentric orbits

For eccentric orbits, $0<e<1$, and the radial motion is bounded by the periastron $r_p|_{min}=pM/(1+e)$ and the apastron $r_p|_{max}=pM/(1-e)$. In Fig. 5 and Fig 6 we display waveforms for two cases: $p=12$ and $e=0.2$, as well as $p=7.801$ and $e=0.9$.

This type of orbital motion generates gravitational waveforms that are different in nature and in frequency content from circular orbits. Rather than being emitted uniformly along the orbit, the radiation is now emitted preferably at periastron. As the eccentricity increases the radiation is emitted in short bursts occurring near periastron. In these situa-

TABLE II. Comparison of averaged fluxes for eccentric orbits with Cutler *et al.* for two points in the p-e plane [12]. The two cases presented are (i) $p=7.50478$ and $e=0.188917$, and (ii) $p=8.75455$ and $e=0.764124$.

	Case		Cutler *et al.*	Time domain	Relative difference
(i)	$p=7.50478$	$\langle \dot{E} \rangle$	3.1680×10^{-4}	3.1770×10^{-4}	0.3%
	$e=0.188917$	$\langle \dot{L} \rangle$	5.9656×10^{-3}	5.9329×10^{-3}	0.5%
(ii)	$p=8.75455$	$\langle \dot{E} \rangle$	2.1008×10^{-4}	2.1484×10^{-4}	2.3%
	$e=0.764124$	$\langle \dot{L} \rangle$	2.7503×10^{-3}	2.7932×10^{-3}	1.6%

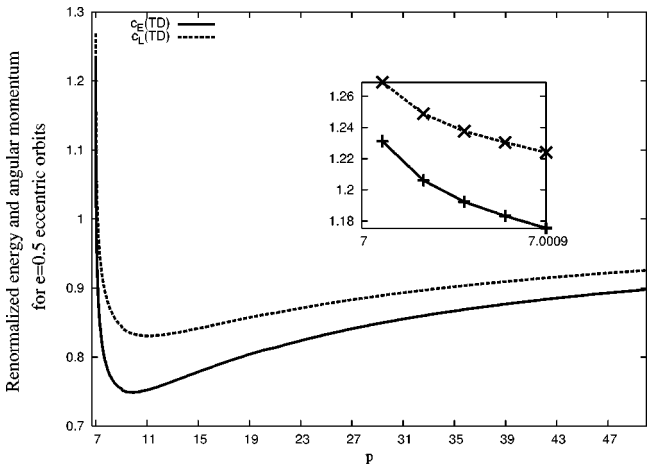

FIG. 7. Coefficients c_E and c_L for the energy and angular momentum radiated as functions of p for $e=0.5$ eccentric orbits. Near the last stable orbit ($p=7$), c_E approaches 1.24, while c_L approaches 1.26.

tions a time-domain approach is far more efficient than a frequency-domain approach. The reason is that in order to correctly calculate the waveforms in the frequency domain, a large number of individual frequencies (harmonics of the radial and azimuthal frequencies) are required, and summing over them can be hugely expensive. By contrast, a time-domain method handles all frequencies simultaneously.

The fluxes are calculated over a number of wave cycles according to

$$\langle \dot{E} \rangle = \frac{1}{T} \int_0^T \dot{E} dt, \tag{3.12}$$

where T is a few (>3) radial periods; a similar expression holds for $\langle \dot{L} \rangle$. To obtain a quantitative idea of the relative accuracy of the time-domain method for eccentric orbits, we compute the fluxes for two points in the p-e plane and compare our calculations with those of Cutler *et al.* [12]: (i) $p=7.50478$ and $e=0.188917$, and (ii) $p=8.75455$ and $e=0.764124$. The results are displayed in Table II. For small eccentricities, e.g. case (i), the agreement is similar to the agreement achieved for circular orbits. For large eccentricities, e.g. case (ii), the agreement is $\sim 2\%$. Because eccentric orbits in Schwarzschild space are characterized by two incommensurate frequencies, the gravitational waveforms are quasi-periodic. By working in the frequency domain, Cutler *et al.* were able to formally average their fluxes over an infinite time. It is not, of course, possible to perform such an average in the time domain. Rather, for high eccentricities, the fluxes are averaged over a limited number of radial cycles (~ 3). This difference in averaging the fluxes is the most likely source of disagreement between time-domain and frequency-domain calculations for case (ii). For case (i), this is not as much of an issue, since the radial period is short enough to allow the time average to be performed over 10 cycles or more.

Finally, we calculate the total energy and angular momentum emitted during one radial period as functions of p for $e=0.5$. We express the total energy and angular momentum radiated to infinity, as calculated from the time domain code, as

$$E_{GR}(p,e) = c_E[E_Q(p,e) + (N-1)E_Q(p/(1+e),0)],$$
$$L_{GR}(p,e) = c_L[L_Q(p,e) + (N-1)L_Q(p/(1+e),0)], \tag{3.13}$$

where we use $E_{GR} = P(p,e)\langle \dot{E} \rangle$, $P(p,e)$ is the radial period of the orbit obtained by integrating Eq. (2.3) over $0 \leqslant \chi \leqslant 2\pi$, $\langle \dot{E} \rangle$ is given by Eq. (3.12), $N = N(p,e)$ is given by Eq. (2.5) with $e=0.5$, $\dot{E}_Q(p,e)$ and $\dot{L}_Q(p,e)$ are given by Eq. (3.9), and c_E and c_L are parameters that stay close to 1 for all values of p. In Fig. 7 we display c_E and c_L as functions of p for $e=0.5$. The coefficient c_E is close to 0.9 for large p and approaches 1.24 for p near 7. Similarly, the coefficient c_L stays close to 0.95 for large p and approaches 1.26 for p near 7. The formulas above for the total energy and angular momentum radiated by a particle in eccentric orbit are justified by the fact that they have the correct lim-

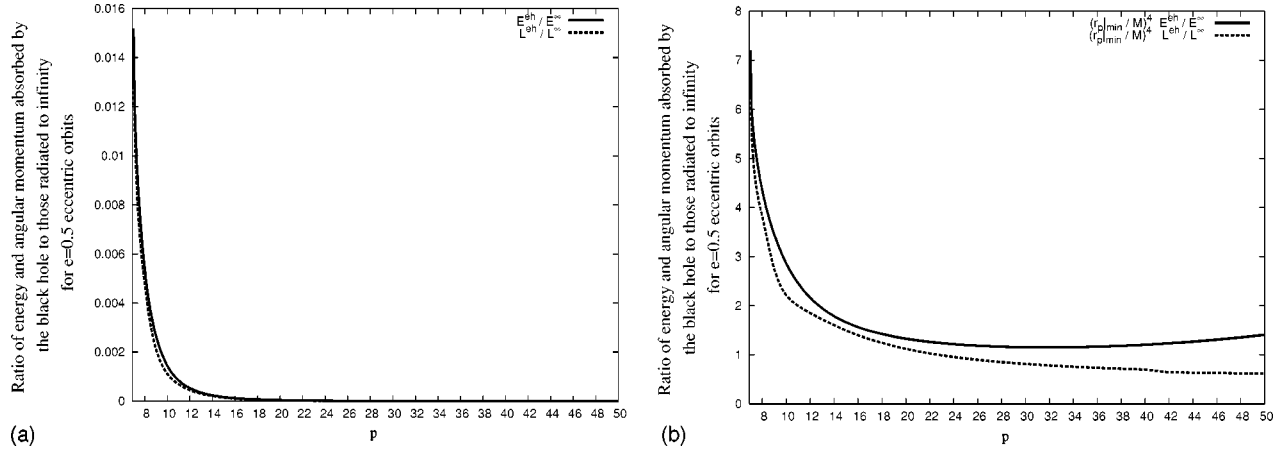

FIG. 8. Black hole absorption for a particle in an $e=0.5$ eccentric orbit. The absorption of both energy and angular momentum is negligible until the particle reaches $p \approx 7.3$, at which point it contributes approximately 1–2 % of the total fluxes; these are eccentric orbits whose periastron is smaller than $4.9M$. The right panel displays the same ratio normalized by $(M/r_p|_{min})^4$.

iting behavior both for p large and for $p \to 6+2e$. For large p, the total energy and angular momentum radiated by a particle on an eccentric orbit are well approximated by the quadrupole formulas given by Eq. (3.7). In this limit, $N \to 1$ and Eq. (3.13) produce the correct approximate energy and angular momentum radiated. When $p \to 6+2e$, the particle orbits the black hole for a number $N-1$ of quasi-circular orbits whose radius is equal to the periastron radius $r_p = Mp/(1+e)$. In this limit N is large and the second term of Eq. (3.13) dominates the energy and angular momentum radiated. This term corresponds to the energy and angular momentum radiated after N such quasi-circular orbits

The frequency of the radiation emitted by the orbiting particle increases as the periastron of the orbit becomes smaller. Since for a given eccentricity e, the periastron is proportional to p, the frequency of the radiation increases with decreasing p. Because the potential barrier around the Schwarzschild black hole is less opaque to high-frequency gravitational waves, we expect an increase in black hole absorption with a decrease in p. This is confirmed numerically for $e=0.5$ and displayed in Fig. 8. For $p \lesssim 7.3$ ($r_p \approx 4.9M$), the absorption of energy and angular momentum by the black hole contributes more than 1% of the total fluxes, while for $p \gtrsim 7.3$ it contributes less than 1% and can be ignored when determining the total fluxes. In the right panel of the figure, we display black hole absorption for $e=0.5$, normalized by $(M/r_p|_{min})^4$, where $r_p|_{min} = Mp/(1+e)$ is the periastron distance. This is the correction expected from black hole absorption for a particle in *circular* orbit at $r_p|_{min}$. We use this normalization here because black hole absorption for generic orbits has not been calculated analytically. For large p, black hole absorption for $e=0.5$ does not seem to converge toward the slow-motion and weak-field approximation for circular orbits. The normalized energy stays above 1, while the normalized angular momentum curve stays below 1. But because the relation $dE = \Omega dL$ used in deriving black hole absorption for circular orbits does not hold in general, there is no reason to believe that $(M/r_p|_{min})^4$ should hold for generic orbits. Determining the differences in black hole absorption due to a finite eccentricity in a weak-field and slow-motion approximation would require a more detailed analysis than ours, since it is in this regime that our determination of black hole absorption is the least accurate.

For radiation emitted by a particle whose orbital parameters are $p=6+2e$ and $0 \leqslant e \leqslant 1$, the argument relating black hole absorption to the orbital separation suggests that black hole absorption should be an increasing function of e along the line $p=6+2e$ ($r_p|_{min}$ is a decreasing function of e along this line). It then comes as no surprise that numerical results displayed in Fig. 9 support this assertion (we used $p=6.001+2e$). Along this line, the radiation is emitted principally at periastron, where the orbit is quasi-circular. The relation $dE = \Omega dL$, where $\Omega = (M/r_p|_{min})^{1/2}$ is the angular velocity of a particle on a circular orbit at $r_p|_{min}$, holds approximately and we find $E^{eh}/E^{\infty} \approx L^{eh}/L^{\infty}$.

E. Parabolic orbits

Particles on a parabolic trajectory have $e=1$ (equivalently $\tilde{E}=1$), and p specifies the value of the periastron: $r_p|_{min} = Mp/2$ with $p>8$. For large values of p, the particle does not spend much time around $r_p|_{min}$, the position where the radiation is maximum; the waveforms have a simple structure around $t=0$, the time at which the radiation emitted at $r_p|_{min}$ reaches an observer at r^*_{obs}. This is displayed for even and odd modes in Fig. 10. In contrast, when p approaches its minimum value ($p_{min} \gtrsim 8$), the particle circles the black hole for a number N of cycles. Because N diverges at $p=8$, we get the zoom-whirl behavior displayed in Fig. 1 [11]. The quasi-circular nature of the motion when r_p approaches $r_p|_{min}$ results in a number of oscillations in the waveforms; these occur near $t=0$ for the observer at r^*_{obs}, and are displayed in Fig. 11 for $p=8.001$.

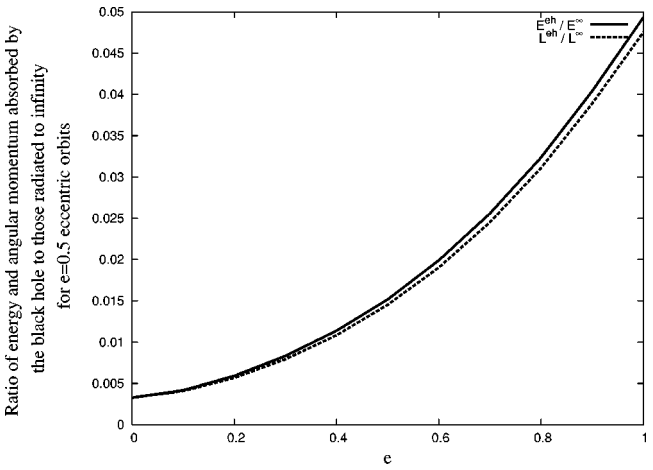

FIG. 9. Displayed are E^{eh}/E^{∞} and L^{eh}/L^{∞} as functions of eccentricity along the curve $p=6.001+2e$. Because of the decrease in periastron distance with increasing e, black hole absorption increases with e. A good approximation to these curves is given by $E^{eh}/E^{\infty} = (1+14e^2)(E^{eh}/E^{\infty})|_{e=0}$.

In similarity with eccentric orbits, we express the numerically calculated energy and angular momentum radiated as

$$E_{GR}(p,e) = c_E[E_Q(p,e) + (N-1)E_Q(p/(1+e),0)],$$
$$L_{GR}(p,e) = c_L[L_Q(p,e) + (N-1)L_Q(p/(1+e),0)], \tag{3.14}$$

where $N=N(p,e)$ is given by Eq. (2.5) with $e=1$, $\dot{E}_Q(e,p)$ and $\dot{L}_Q(e,p)$ are given by Eq. (3.9), and c_E and c_L are again parameters that stay close to 1 for all p. For parabolic orbits, the total energy and angular momentum are computed using Eqs. (3.5) and (3.6) as

$$E^{\infty}_{GR} = \int_{-T}^{T} \dot{E}^{\infty} dt,$$
$$L^{\infty}_{GR} = \int_{-T}^{T} \dot{L}^{\infty} dt, \tag{3.15}$$

for T large [we used $T=300(2M)$]. In Fig. 12, we display c_E and c_L for parabolic orbits. These quantities are close to 1 for large p, but increase above 1 as p approaches 8. Near this value of p, c_E reaches 1.81, while c_L approaches 1.84. As for

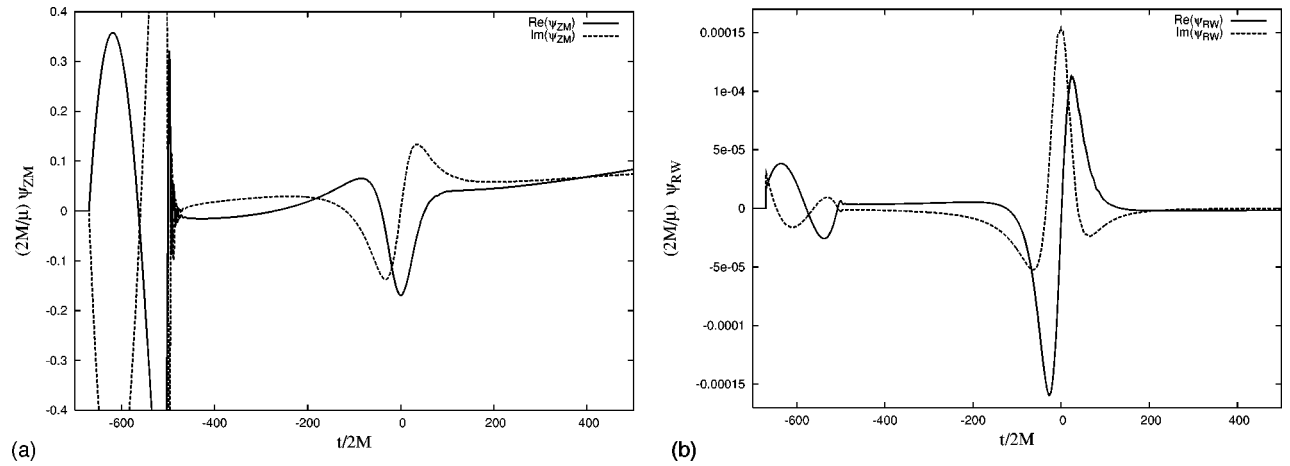

FIG. 10. Displayed are ψ_{ZM} (left, $l=2,m=2$) and ψ_{RW} (right, $l=2,m=1$) as functions of time for $e=1$ and $p=40$. As in the case of circular orbits, early times are dominated by the initial data content. Total energy and angular momentum are calculated in the range $-300\leqslant t/2M\leqslant 300$.

eccentric orbits, we find that for large p the energy and angular momentum approach the values given by the quadrupole approximation, but that for p close to $6+2e$ they are better approximated by the energy and angular momentum radiated by a particle orbiting the black hole N times on a circular orbit of radius $r_p|_{min}=Mp/(1+e)$.

The argument given previously for eccentric orbits holds true for parabolic orbits: when $p\gtrsim 8$, black hole absorption is more important than for circular or eccentric orbit (see Fig. 9). Our numerical results show that for $p>10$, E^{eh} and L^{eh} account for less than 1% of the total energy and angular momentum radiated, while for $p\lesssim 10$ they can contribute as much as 5% of the total amounts (see Fig. 13). Hence, for $p\lesssim 10$, black hole absorption contributes a few percent of the total energy and angular momentum radiated and needs to be included in an accurate computation. Black hole absorption is not determined as accurately as the energy and angular momentum radiated to infinity, but the error we make in evaluating it is never large enough to spoil our goal of $\sim 1\%$ overall accuracy.

For completeness, in Table III we display $E_{GR}^{\infty,eh}$ and $L_{GR}^{\infty,eh}$, the total energy and angular momentum radiated to infinity and through the event horizon, as returned by the time-domain code, for a wide range of p values. Based on the accuracy obtained for circular and eccentric orbits, we estimate that the total energy and angular momentum lost to gravitational waves are calculated to a relative accuracy of 1–2 %. The actual accuracy is likely to be close to the accuracy achieved for circular orbits. The reason for this is quite simple. For parabolic orbits, there is no issue of performing a time average, since the particle passes through periastron only once and we calculate the total energy for that motion.

IV. CONCLUSION

The time-domain method can produce waveforms and compute the associated fluxes of energy and angular momentum to a relative accuracy of a few percent. For circular orbits, the method is extremely reliable and produces fluxes with an overall accuracy of 1% or better over the whole

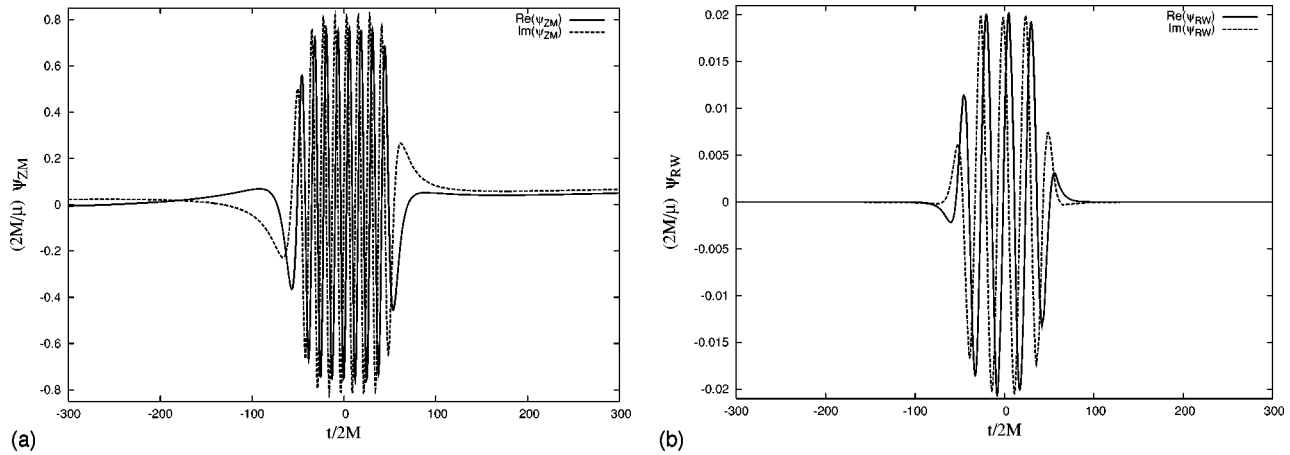

FIG. 11. Displayed are ψ_{ZM} (left, $l=2,m=2$) and ψ_{RW} (right, $l=2,m=1$) as functions of time for $e=1$ and $p=8.001$. Early times, where the choice of initial data dominates, are not displayed in order to make the $t=0$ region clearly visible. The energy and angular momentum fluxes are integrated in the range $-300\leqslant t/2M\leqslant 300$ to obtain the total energy and angular momentum radiated.

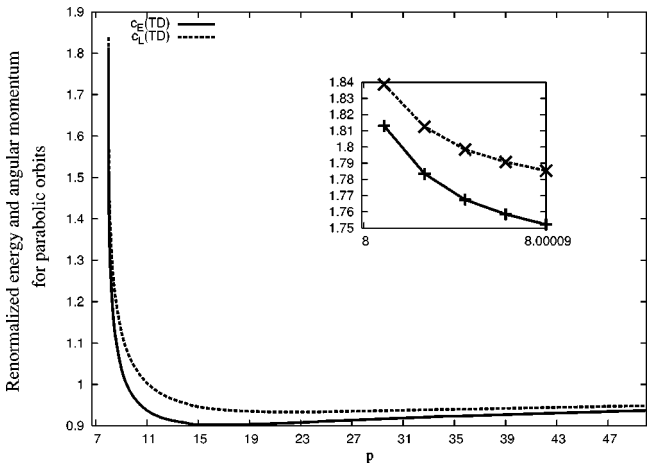

FIG. 12. Coefficients c_E and c_L for the total energy and angular momentum radiated as functions of p for a particle in parabolic orbit. Near $p=8$, c_E approaches 1.81 while c_L approaches 1.84.

range of p values explored. For eccentric orbits, the comparison with the results of Cutler *et al.* [12] is spoiled by the difficulty in performing a time average of the fluxes over a sufficiently long time. Because the disagreement arises from the differences in time averaging, the time-domain method is still capable of producing accurate waveforms for highly eccentric motion. We stress here that the limitation is in the computation of the time-averaged fluxes, not in obtaining the waveforms. On the other hand, for geodesics with small eccentricities there is no such limitation and the time-domain results are in better agreement with those calculated by Cutler *et al.* [12]. In all cases, the time-domain method is capable of determining the fluxes accurately to 1–2 %. Similar accuracy is obtained for the total energy and angular momentum radiated by a particle traveling on a parabolic orbit.

We also computed the absorption of energy and angular momentum by the black hole. For circular orbits with $p>6$, this contribution can always be neglected, but not for orbits whose periastron is smaller than $5M$. For such orbits, black hole absorption contributes more than 1% of the total fluxes and cannot be ignored. We showed that for $e=0.5$ it can constitute a correction as large as 2% of the total fluxes; for parabolic orbits the contribution increases to 5%.

ACKNOWLEDGMENTS

This work was supported in part by the Natural Sciences and Engineering Research Council of Canada. The author gratefully acknowledges the help of Eric Poisson and his comments on previous versions of this paper.

APPENDIX A: A SHORT REVIEW OF BLACK HOLE PERTURBATION THEORY

Since the pioneering work of Regge and Wheeler [8] and Zerilli [6], perturbations of the Schwarzschild black hole have been studied extensively. Here we provide a short summary of the formalism, including the source terms appropriate for the Zerilli-Moncrief and Regge-Wheeler equations.

The perturbations of the Schwarzschild spacetime are described by a linear perturbation tensor $h_{\mu\nu}=g_{\mu\nu}-g_{\mu\nu}^{Schwarzschild}$, where $g_{\mu\nu}$ is the metric of the perturbed spacetime and $g_{\mu\nu}^{Schwarzschild}$ the Schwarzschild solution. This tensor is written as a multipole expansion using scalar, vectorial, and tensorial spherical harmonics. In Schwarzschild coordinates, we have

$$
\begin{aligned}
&h_{tt}=fH_0(t,r)Y^{lm}, \quad h_{tr}=H_1(t,r)Y^{lm},\\
&h_{rr}=fH_2(t,r)Y^{lm},\\
&h_{tA}=q_0(t,r)Z_A^{lm}+h_0(t,r)X_A^{lm},\\
&h_{rA}=q_1(t,r)Z_A^{lm}+h_1(t,r)X_A^{lm},\\
&h_{AB}=r^2[K(t,r)U_{AB}^{lm}+G(t,r)V_{AB}^{lm}]+h_2(t,r)W_{AB}^{lm},
\end{aligned}
\tag{A1}
$$

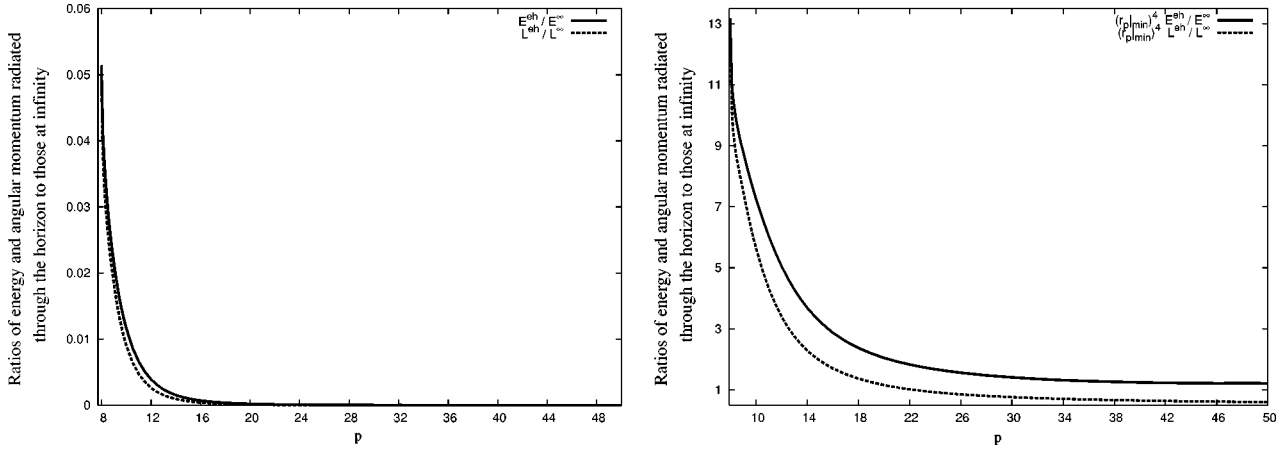

FIG. 13. Black hole absorption for a particle following a parabolic geodesic. The absorption of both energy and angular momentum is negligible until the particle reaches $p\approx 10$ or $r_p|_{min}\approx 5M$. The right panel displays the same ratio normalized by $(M/r_p|_{min})^4$, where $r_p|_{min}$ is the radii at periastron. Again, this factor is meaningful only for circular orbits, and is used only to illustrate the behavior of black hole absorption as a function of p.

TABLE III. Total energy and angular momentum radiated by a particle orbiting a Schwarzschild black hole in a parabolic orbit. As usual, E^{∞}_{GR} and L^{∞}_{GR} denote the energy and angular momentum radiated to infinity, while E^{eh}_{GR} and L^{eh}_{GR} are the energy and angular momentum absorbed by the black hole. The black hole absorption contributes to less than 1% when $p \gtrsim 10$: for parabolic orbits with periastron smaller than $5M$, black hole absorption contributes a significant amount to the total energy and angular momentum radiated.

p	E^{∞}_{GR}	E^{eh}_{GR}	L^{∞}_{GR}	L^{eh}_{GR}
8.00001	3.6703	1.8876×10^{-1}	3.0133×10	1.5208
8.001	2.2809	1.1260×10^{-1}	1.9088×10	9.1166×10^{-1}
8.201	7.1130×10^{-1}	2.6586×10^{-2}	6.6010	2.2142×10^{-1}
8.401	5.1740×10^{-1}	1.6534×10^{-2}	5.0433	1.4244×10^{-1}
8.601	4.0970×10^{-1}	1.1376×10^{-2}	4.1665	1.0148×10^{-1}
8.801	3.3767×10^{-1}	8.1988×10^{-3}	3.5706	7.5175×10^{-2}
9.0	2.8419×10^{-1}	6.0880×10^{-3}	3.1196	5.7026×10^{-2}
9.2	2.4409×10^{-1}	4.6044×10^{-3}	2.7756	4.3891×10^{-2}
9.4	2.1228×10^{-1}	3.5352×10^{-3}	2.4973	3.4211×10^{-2}
9.6	1.8644×10^{-1}	2.7473×10^{-3}	2.2665	2.6951×10^{-2}
9.8	1.6506×10^{-1}	2.1565×10^{-3}	2.0718	2.1428×10^{-2}
10.0	1.4712×10^{-1}	1.7072×10^{-3}	1.9048	1.7176×10^{-2}
10.5	1.1292×10^{-1}	9.8226×10^{-4}	1.5752	1.0193×10^{-2}
11.0	8.8979×10^{-2}	5.8626×10^{-4}	1.3320	6.2819×10^{-3}
11.5	7.1545×10^{-2}	3.6067×10^{-4}	1.1455	3.9971×10^{-3}
12.0	5.8467×10^{-2}	2.2778×10^{-4}	9.9827×10^{-1}	2.6152×10^{-3}
12.5	4.8424×10^{-2}	1.4732×10^{-4}	8.7936×10^{-1}	1.7546×10^{-3}
13.0	4.0567×10^{-2}	9.7321×10^{-5}	7.8158×10^{-1}	1.2036×10^{-3}
13.5	3.4326×10^{-2}	6.5582×10^{-5}	7.0011×10^{-1}	8.4286×10^{-4}
14.0	2.9303×10^{-2}	4.4999×10^{-5}	6.3136×10^{-1}	6.0123×10^{-4}
14.5	2.5134×10^{-2}	3.1409×10^{-5}	5.7133×10^{-1}	4.3635×10^{-4}
15.0	2.1774×10^{-2}	2.2273×10^{-5}	5.2088×10^{-1}	3.2171×10^{-4}
16.0	1.6636×10^{-2}	1.1675×10^{-5}	4.3867×10^{-1}	1.8241×10^{-4}
17.0	1.2978×10^{-2}	6.4484×10^{-6}	3.7499×10^{-1}	1.0869×10^{-4}
18.0	1.0303×10^{-2}	3.7241×10^{-6}	3.2454×10^{-1}	6.7569×10^{-5}
19.0	8.3029×10^{-3}	2.2354×10^{-6}	2.8383×10^{-1}	4.3565×10^{-5}
20.0	6.7794×10^{-3}	1.3882×10^{-6}	2.5047×10^{-1}	2.8990×10^{-5}
22.0	4.6735×10^{-3}	5.8355×10^{-7}	1.9949×10^{-1}	1.3895×10^{-5}
24.0	3.3426×10^{-3}	2.6965×10^{-7}	1.6280×10^{-1}	7.2550×10^{-6}
26.0	2.4638×10^{-3}	1.3447×10^{-7}	1.3549×10^{-1}	4.0539×10^{-6}
28.0	1.8620×10^{-3}	7.1373×10^{-8}	1.1459×10^{-1}	2.3931×10^{-6}
30.0	1.4374×10^{-3}	3.9949×10^{-8}	9.8213×10^{-2}	1.4781×10^{-6}
32.0	1.1298×10^{-3}	2.3372×10^{-8}	8.5141×10^{-2}	9.4827×10^{-7}
34.0	9.0223×10^{-4}	1.4201×10^{-8}	7.4534×10^{-2}	6.2832×10^{-7}
36.0	7.2956×10^{-4}	8.9299×10^{-9}	6.5744×10^{-2}	4.2804×10^{-7}
38.0	5.9799×10^{-4}	5.7886×10^{-9}	5.8484×10^{-2}	2.9873×10^{-7}
40.0	4.9549×10^{-4}	3.8422×10^{-9}	5.2369×10^{-2}	2.1296×10^{-7}
42.0	4.1455×10^{-4}	2.6163×10^{-9}	4.7168×10^{-2}	1.5469×10^{-7}
44.0	3.4987×10^{-4}	1.8214×10^{-9}	4.2706×10^{-2}	1.1427×10^{-7}
46.0	2.9763×10^{-4}	1.2887×10^{-9}	3.8849×10^{-2}	8.5683×10^{-8}
48.0	2.5501×10^{-4}	9.3316×10^{-10}	3.5491×10^{-2}	6.5130×10^{-8}
50.0	2.1993×10^{-4}	6.8343×10^{-10}	3.2550×10^{-2}	5.0118×10^{-8}

where capital roman indices run over the angular coordinates (θ,φ), $f=1-2M/r$, and Y^{lm} are the usual scalar harmonics, in terms of which the vectorial and tensorial spherical harmonics are defined as

$$Z^{lm}_{A}=Y^{lm}_{|A}, \quad X^{lm}_{A}=\varepsilon^{B}_{A}Y^{lm}_{|B}, \quad U^{lm}_{AB}=\Omega_{AB}Y^{lm},$$

$$V^{lm}_{AB}=Y^{lm}_{|AB}+\frac{l(l+1)}{2}\Omega_{AB}Y^{lm}, \quad \text{and} \quad W^{lm}_{AB}=X^{lm}_{(A|B)}.$$

Here $\Omega_{AB}=(1,\sin^2\theta)$, a bar denotes the covariant derivative compatible with Ω_{AB}, and ε_{AB} is the Levi-Cività tensor on

the unit two-sphere. The coefficients of the multipole expansions have implicit l and m indices, and there is an implicit summation over these indices. Defined this way, H_0, H_1, H_2, q_0, q_1, K and G are even parity modes, while h_0, h_1 and h_2 are odd parity modes.

By construction, the vectorial and tensorial spherical harmonics obey $S^{l,-m}=(-)^m S^{lm}*$, where S is any spherical harmonic function. (This relation holds for scalar spherical harmonics, and since vectorial and tensorial spherical harmonics are obtained by the action of *real* operators on Y^{lm}, it also applies to these functions.) An important consequence of this relation is that for real metric perturbations, the multipole moments must satisfy $M^{l,-m}=(-)^m M^{lm}*$, where M^{lm} is any one of H_0, H_1, H_2, q_0, q_1, K, G, h_0, h_1, and h_2. It is then easily established that $M^{lm}M^{*lm}=M^{l,-m}M^{*l,-m}$. This justifies folding the $m<0$ terms over to $m>0$ in Eqs. (3.5) and (3.6).

A gauge transformation can be used to eliminate four of the metric perturbations. In the Regge-Wheeler gauge, this freedom is used to set $q_0=q_1=G=0$, and $h_2=0$. The two scalar fields

$$\psi_{ZM}=\frac{r}{\lambda+1}\left[K+\frac{f}{\Lambda}\left(H_2-r\frac{\partial}{\partial r}K\right)\right], \tag{A2}$$

$$\psi_{RW}=-\frac{f}{r}h_1, \tag{A3}$$

where $\lambda=(l+2)(l-1)/2$ and $\Lambda=\lambda+3M/r$ are the Zerilli-Moncrief and Regge-Wheeler functions, respectively. Their evolution is governed by Eq. (1.1) with the potentials

$$V_{ZM}=\frac{f}{r^2\Lambda^2}\left[2\lambda^2\left(\lambda+1+\frac{3M}{r}\right)+\frac{18M^2}{r^2}\left(\lambda+\frac{M}{r}\right)\right],$$

$$V_{RW}=\frac{f}{r^2}\left[l(l+1)-\frac{6M}{r}\right], \tag{A4}$$

and the source terms

$$S_{ZM}=\frac{1}{(\lambda+1)\Lambda}\left\{r^2 f\left(f^2\frac{\partial}{\partial r}Q^{tt}-\frac{\partial}{\partial r}Q^{rr}\right)+r(\Lambda-f)Q^{rr}+rf^2Q^{\flat}-\frac{f^2}{r\Lambda}[\lambda(\lambda-1)r^2+(4\lambda-9)Mr+15M^2]Q^{tt}\right\}+\frac{2f}{\Lambda}Q^r-\frac{f}{r}Q^{\sharp},$$

$$S_{RW}=\frac{f}{r}\left[\frac{2}{r}\left(1-\frac{3M}{r}\right)P-f\frac{\partial}{\partial r}P+P^r\right].$$

These are constructed from the perturbing stress-energy tensor $T^{\mu\nu}$ and we have defined

$$Q^{ab}=8\pi\int T^{ab}Y^{lm}*d\Omega,\quad Q^a=\frac{16\pi r^2}{l(l+1)}\int T^{aA}Z_A^{lm}*d\Omega,$$

$$Q^{\flat}=8\pi r^2\int T^{AB}U_{AB}^{lm}*d\Omega,$$

$$Q^{\sharp}=\frac{32\pi r^4}{(l-1)l(l+1)(l+2)}\int T^{AB}V_{AB}^{lm}*d\Omega,$$

and

$$P^a=\frac{16\pi r^2}{l(l+1)}\int T^{aA}X_A^{lm}*d\Omega,$$

$$P=\frac{16\pi r^4}{(l-1)l(l+1)(l+2)}\int T^{AB}W_{AB}^{lm}*d\Omega;$$

lower-case roman indices run over t and r, the integration is over the unit two-sphere with $d\Omega=\sin\theta d\theta d\varphi$, and T^{ab}, T^{aA} and T^{AB} are components of $T^{\mu\nu}$. For a particle traveling on a geodesic with proper time τ, coordinates $z_p^\mu(\tau)$, and four-velocity $u^\mu(\tau)$, the stress-energy tensor is

$$T^{\mu\nu}=\mu\int d\tau(-g)^{-1/2}u^\mu u^\nu\delta^4[x^\alpha-z_p^\alpha], \tag{A5}$$

where $\delta^4[x^\alpha-z^\alpha]$ is a four-dimensional Dirac functional.

These expressions for the source terms can be used, combined with the geodesic equations of the Schwarzschild spacetime, to calculate explicit expressions for the factors $G(t,r)$ and $F(t,r)$ appearing in Eq. (1.2). For even parity modes (ZM), we get

$$G(r,t)=aY^*(t)+bZ_\varphi^*(t)+cU_{\varphi\varphi}^*(t)+dV_{\varphi\varphi}^*(t),$$

$$F(r,t)=\frac{8\pi}{\lambda+1}\frac{f^2}{\Lambda}\frac{\tilde{V}^2}{\tilde{E}}Y^*(t), \tag{A6}$$

where $\tilde{V}^2=f(1+\tilde{L}^2/r^2)$,

$$a=\frac{8\pi}{\lambda+1}\frac{f^2}{r\Lambda^2}\left\{\frac{6M}{r}\tilde{E}-\frac{\Lambda}{\tilde{E}}\left[\lambda+1-\frac{3M}{r}+\frac{\tilde{L}^2}{r^2}\left(\lambda+3-\frac{7M}{r}\right)\right]\right\},$$

and

$$b=\frac{16\pi}{\lambda+1}\frac{\tilde{L}}{\tilde{E}}\frac{f^2}{r^2\Lambda}u^r,\quad c=\frac{8\pi}{\lambda+1}\frac{\tilde{L}^2}{\tilde{E}}\frac{f^3}{r^3\Lambda},$$

$$d=-32\pi\frac{(l-2)!}{(l+2)!}\frac{\tilde{L}^2}{\tilde{E}}\frac{f^2}{r^3}.$$

Finally, the source terms for odd parity modes (RW) are

$$G(r,t)=\frac{f^2}{r^3}\left[\frac{4}{r}\left(1-\frac{3M}{r}\right)\alpha+\beta\right],$$

$$F(r,t)=-\alpha\frac{f^3}{r^3}, \tag{A7}$$

where

$$\alpha=16\pi\frac{(l-2)!}{(l+2)!}\frac{\tilde{L}^2}{\tilde{E}}W^{*lm}_{\varphi\varphi}(t),\quad \beta=\frac{8\pi}{\lambda+1}\frac{\tilde{L}}{\tilde{E}}u^r X^{*lm}_{\varphi}(t).$$

Note that $G(r,t)$ and $F(r,t)$ contain scalar, vectorial and tensorial harmonic functions evaluated at the angular position of the particle $\varphi_p(t)$. For example, for even modes, some terms in G and F are proportional to $Y^{lm}(\pi/2,\varphi_p(t))$. Because the orbital motion takes place in the equatorial plane, each spherical harmonic function is evaluated at $\theta_p=\pi/2$. A useful consequence of this is that the source term for the Zerilli-Moncrief function vanishes when $l+m$ is odd, while the source term for the Regge-Wheeler function vanishes when $l+m$ is even. This was used in Eq. (3.3) and Eq. (3.4).

Once ψ_{ZM} and ψ_{RW} are found by solving Eq. (1.1), with the source terms of Eqs. (A6) and (A7), the perturbation tensor can be reconstructed. In the Regge-Wheeler gauge, we have

$$K=f\frac{\partial}{\partial r}\psi_{ZM}+A(r)\psi_{ZM}-\frac{r^2f^2}{(\lambda+1)\Lambda}Q^{tt},$$

$$H_2=\frac{\Lambda}{f}\left[\frac{\lambda+1}{r}\psi_{ZM}-K\right]+r\frac{\partial}{\partial r}K,$$

$$H_1=r\frac{\partial}{\partial t}\left[\frac{\partial}{\partial r}\psi_{ZM}+B(r)\psi_{ZM}\right]-\frac{r^2}{\lambda+1}\left[Q^{tr}+\frac{rf}{\Lambda}\frac{\partial}{\partial t}Q^{tt}\right],$$

$$H_0=H_2+Q^{\sharp} \tag{A8}$$

for even parity modes, where we have defined $A(r)=[\lambda(\lambda+1)+3M/r(\lambda+2M/r)]/(r\Lambda)$ and $B(r)=[\lambda(1-3M/r)-3M^2/r^2]/(rf\Lambda)$. For odd parity modes, the reconstructed metric perturbations are

$$h_0=-f\int_{-\infty}^{t}dt'\left[\frac{\partial}{\partial r}(r\psi_{RW}(t',r))+P\right],$$

$$h_1=-rf^{-1}\psi_{RW}. \tag{A9}$$

APPENDIX B: RADIATION ZONE FLUXES AND BLACK HOLE ABSORPTION

The fluxes of energy and angular momentum can be obtained from Isaacson's stress-energy tensor for gravitational waves:

$$T^{GW}_{\mu\nu}=\frac{1}{64\pi}\langle h^{\alpha\beta}{}_{;\mu}h_{\alpha\beta;\nu}\rangle, \tag{B1}$$

where $\langle\ldots\rangle$ denotes an average over a region of spacetime large compared with the wavelength of the radiation. Typically, $T_{\mu\nu}$ can be defined when the wavelength of the radiation, λ, is small compared to a typical radius of curvature $\mathcal{R}$. By definition, $\lambda\ll\mathcal{R}$ in the radiation zone and the stress-energy tensor for gravitational waves can be defined there. There is a second region where the condition $\lambda\ll\mathcal{R}$ is satisfied: A stationary observer near $r=2M$ sees $\mathcal{R}\sim 2M$, but the radiation is strongly blueshifted and $\lambda\to 0$; that this is the case is clear from the divergence in Eq. (B30) below.

Because the Schwarzschild black hole is static and axially symmetric, it possesses two Killing vectors, ${}_{(t)}\xi^{\alpha}$ and ${}_{(\varphi)}\xi^{\alpha}$, that can be used, in conjunction with $T_{\mu\nu}$, to obtain expressions for the fluxes of energy and angular momentum through a surface Σ at constant r. We have that (dropping the "GW" on the stress-energy tensor)

$$dE=-\int_{\Sigma}T^{\mu}_{\nu\ (t)}\xi^{\nu}d\Sigma_{\mu}, \tag{B2}$$

$$dL=\int_{\Sigma}T^{\mu}_{\nu\ (\varphi)}\xi^{\nu}d\Sigma_{\mu}, \tag{B3}$$

where $d\Sigma_{\mu}$ is an outward oriented surface element on Σ. In Schwarzschild coordinates, these expressions reduce to

$$\dot{E}=-\epsilon r^2 f\int d\Omega T_{tr},$$

$$\dot{L}=\epsilon r^2 f\int d\Omega T_{r\varphi}, \tag{B4}$$

where an overdot indicates differentiation with respect to t, and ϵ is 1 when calculating the fluxes in the radiation zone and -1 when calculating black hole absorption. Because the event horizon is a null surface, it is conceptually better to use dE/dv and dL/dv in place of dE/dt and dL/dt (with $v=t+r^*$). Similarly, because radiation travels to $\mathcal{J}^+$, which is another null surface, it is conceptually better to use dE/du and dL/du instead of dE/dt and dL/dt for outgoing fluxes (with $u=t-r^*$). However, because we numerically extract the gravitational waveforms at finite values of r^*, without ever reaching the event horizon or $\mathcal{J}^+$, the use of dE/dt and dL/dt is a better representation of our numerical procedure.

We provided a summary of the perturbation formalism in Appendix A. This included explicit formulas to reconstruct the metric perturbations in the Regge-Wheeler gauge. To construct T_{tr} and $T_{r\varphi}$, it proves convenient to extract the radiative part of the perturbation tensor. To this end, we introduce the null tetrad l^{μ}, n^{μ}, and m^{μ}: l^{μ} and n^{ν} are null vectors tangent to outgoing and ingoing rays, respectively, while m^{μ} is a complex null vector (with complex conjugate $\bar{m}^{\mu}$) on the two-sphere. They satisfy the relations

$$l^\mu l_\mu = 0 = n^\mu n_\mu, \quad m^\mu m_\mu = 0 = \bar{m}^\mu \bar{m}_\mu,$$
$$l^\mu n_\mu = -1 = -m^\mu \bar{m}_\mu. \tag{B5}$$

In Schwarzschild coordinates, their components are

$$l_\mu = (-1, f^{-1}, 0, 0), \quad n_\mu = -\frac{1}{2}(f, 1, 0, 0),$$
$$m_\mu = \frac{\sqrt{2}}{2} r(0, 0, 1, \imath \sin\theta). \tag{B6}$$

To find the perturbation tensor in a radiation gauge, we seek a gauge vector ξ^μ that generates the transformation between the Regge-Wheeler gauge and the radiation gauge. Under such an infinitesimal coordinate transformation, the perturbation field transforms as $h^{RG}_{\mu\nu} = h^{RW}_{\mu\nu} - \xi_{(\mu;\nu)}$, where *RG* stands for radiation gauge and *RW* for Regge-Wheeler gauge. Using the spherical harmonic functions introduced previously, the vector ξ^μ can be expressed as a multipole expansion [8]:

$$\xi^{(even)}_\mu = (\alpha_t Y^{lm}, \alpha_r Y^{lm}, r^2 \beta Z^{lm}_A),$$
$$\xi^{(odd)}_\mu = (0, 0, r^2 \kappa X^{lm}_A), \tag{B7}$$

where α_t, α_r, β and κ are freely specifiable gauge functions. Combining this with the multipole expansion for the perturbation tensor in the Regge-Wheeler gauge, we obtain the transformation law for the each perturbation mode:

$$H^{RG}_0 = H^{RW}_0 - 2f^{-1}\left(\dot{\alpha}_t - \frac{M}{r^2} f \alpha_r\right),$$
$$H^{RG}_1 = H^{RW}_1 - \left(\alpha'_t + \dot{\alpha}_r - \frac{2M}{r^2} f^{-1} \alpha_t\right),$$
$$H^{RG}_2 = H^{RW}_2 - 2f\left(\alpha'_r + \frac{M}{r^2} f^{-1} \alpha_r\right),$$
$$q^{RG}_t = -(\alpha_t + r^2 \dot{\beta}),$$
$$q^{RG}_r = -(\alpha_r + r^2 \beta'),$$
$$K^{RG} = K^{RW} - \left(\frac{2f}{r}\alpha_r - l(l+1)\beta\right),$$
$$G^{RG} = -2\beta \tag{B8}$$

for the transformation of even parity modes, and

$$h^{RG}_t = h^{RW}_0 - r^2 \dot{\kappa},$$
$$h^{RG}_r = h^{RW}_1 - r^2 \kappa',$$
$$h^{RG}_2 = -2r^2 \kappa \tag{B9}$$

for odd modes; an overdot designates a t derivative and a prime an r derivative. In the next two subsections, we develop solutions appropriate to outgoing and ingoing radiation gauges, respectively.

1. Outgoing radiation gauge

In an outgoing radiation gauge $h^{ORG}_{\mu\nu}$, the perturbation tensor satisfies [23]

$$h^{ORG}_{\mu\nu} n^\mu n^\nu = 0,$$
$$h^{ORG}_{\mu\nu} n^\mu m^\nu = 0 = h^{ORG}_{\mu\nu} n^\mu \bar{m}^\nu,$$
$$h^{ORG}_{\mu\nu} n^\mu l^\nu = 0 = h^{ORG}_{\mu\nu} m^\mu \bar{m}^\nu. \tag{B10}$$

The first two conditions indicate the $h^{ORG}_{\mu\nu}$ is transverse to outgoing null rays, while the last condition indicates that it is traceless. Equations (B10) involve five conditions, one too many for the specification of a gauge. But this system is not overdetermined: once four of these equations are enforced, the fifth is found to be satisfied automatically in the radiation zone.

From Eqs. (B8) and (B9), the gauge conditions can be expressed in terms of multipole moments. To leading order in r^{-1}, we get

$$4(\dot{\alpha}_t - \dot{\alpha}_r) = H^{RW}_0 + H^{RW}_2 - 2H^{RW}_1,$$
$$\alpha_t - \alpha_r + 2r^2 \dot{\beta} = 0,$$
$$\dot{\alpha}_t + \dot{\alpha}_r = 0,$$
$$\frac{2}{r}\alpha_r = -K^{\mathrm{RW}} \tag{B11}$$

for even parity modes, and

$$2r^2 \dot{\kappa} = h^{RW}_1 - h^{RW}_0 \tag{B12}$$

for odd parity modes. We used $\partial/\partial t = -\partial/\partial r + \mathcal{O}(r^{-1})$, appropriate in the radiation zone, to eliminate r derivatives in favor of t derivatives.

The right-hand side of these equations contains the perturbation tensor in the Regge-Wheeler gauge. From Eq. (A8), we find that, in the radiation zone, even parity modes have the asymptotic form

$$K^{RW} \approx -\dot{\psi}_{ZM}, \quad H^{RW}_2 \approx H^{RW}_0 \approx -H^{RW}_1 \approx r\ddot{\psi}_{ZM},$$

while, from Eq. (A9), we find that odd parity modes are given asymptotically by

$$h_0 \approx -h_1 \approx r\psi_{RW}.$$

Solutions to the gauge transformation are then easy to

find. For even modes, the last of Eq. (B11) yields $\alpha_r = -(1/2)r\dot{\psi}_{ZM}$. The other gauge functions are easily obtained from the remaining equations of Eq. (B11): $\alpha_t = -\alpha_r$ and $\beta = -\psi_{ZM}/(2r)$. For odd modes, direct integration of Eq. (B12) yields $\kappa = 1/r\int_{-\infty}^{t} dt'\,\psi_{RW}(t')$. Going back to Eqs. (B8) and (B9), we can reconstruct the perturbation tensor in the radiation zone. Solving these for G^{ORG} and h_2^{ORG}, we get

$$h_{AB}^{ORG} = r\left(\psi_{ZM}(t)V_{AB}^{lm} - 2\int_{-\infty}^{t} dt'\,\psi_{RW}(t')W_{AB}^{lm}\right) + \mathcal{O}(1). \tag{B13}$$

In this expression, the Zerilli-Moncrief and Regge-Wheeler functions have l and m multipole indices and there is an implicit summation over them. Dropping the $\mathcal{O}(1)$ term, we refer to h_{AB}^{ORG} as the radiative part of the perturbation tensor in the radiation zone, because it contains all of the information about energy and angular momentum carried to infinity. This last expression can be re-written in terms of the two gravitational-wave polarizations, $h_+ = h_{\theta\theta}^{ORG}/r^2$, and $h_\times = h_{\theta\varphi}^{ORG}/(r^2\sin\theta)$. The result is Eq. (3.1).

2. Ingoing radiation gauge

To obtain the radiative part of the gravitational field in the vicinity of the event horizon, we impose an ingoing radiation gauge. We seek a solution to leading order in $f \to 0$, the expansion parameter near the horizon.

The ingoing radiation gauge can be obtained from Eq. (B10), by making the replacement $l^\mu \leftrightarrow n^\mu$ of the tetrad vectors. The same comment about the number of gauge conditions can be made here: only four gauge conditions need to be imposed, and the fifth condition is then satisfied automatically.

From Eq. (B8), Eq. (B9), and the ingoing radiation gauge conditions, we obtain

$$\begin{aligned}
&4(\dot{\alpha}_t + \dot{\alpha}_r) - \frac{1}{M}(\alpha_t + \alpha_r) = 2f(H_2^{RW} + H_1^{RW}),\\
&\dot{\alpha}_t - \dot{\alpha}_r = 0,\\
&8M^2\dot{\beta} + \alpha_t + \alpha_r = 0,\\
&\frac{1}{M}\alpha_r - \beta = K^{RW}
\end{aligned} \tag{B14}$$

for the gauge transformation of even parity modes, and

$$r^2\dot{\kappa} = r(h_0^{RW} + fh_1^{RW}) \tag{B15}$$

for odd parity modes: we substituted $\alpha_r \to f^{-1}\alpha_r$ in Eq. (B8), we used $\partial/\partial r^* = \partial/\partial t + \mathcal{O}(f)$ to eliminate derivatives with respect to r^*, and an overdot denotes a time derivative.

The asymptotic form of the metric perturbations in the Regge-Wheeler gauge is obtained from Eqs. (A8) and (A9). We get

$$K^{RW} \approx \dot{\psi}_{ZM} + \frac{\lambda+1}{2M}\psi_{ZM},$$

$$H_2^{RW} = H_0^{RW} = H_1^{RW} = f^{-1}\left(2M\ddot{\psi}_{ZM} - \frac{1}{2}\dot{\psi}_{ZM}\right)$$

for even parity modes, and

$$h_0^{RW} = fh_1^{RW} = -2M\psi_{RW}$$

for odd parity ones. These can be inserted back into Eqs. (B14) and (B15). The solution to the gauge transformation then proceeds as follow. For even parity modes, the second and third equations yield $\alpha_r = \alpha_t$ and $4M^2\dot{\beta} = -\alpha_t$. These can be substituted into the first and the time derivative of the fourth of Eq. (B14), to yield a system of equation for α_t:

$$\dot{\alpha}_t - \frac{1}{4M}\alpha_t = M\ddot{\psi}_{ZM} - \frac{1}{4}\dot{\psi}_{ZM}, \tag{B16}$$

$$\dot{\alpha}_t + \frac{\lambda+1}{2M}\alpha_t = M\ddot{\psi}_{ZM} + \frac{\lambda+1}{2}\dot{\psi}_{ZM}. \tag{B17}$$

Eliminating the time derivative by subtraction, we find $\alpha_t = M\dot{\psi}_{ZM}$. For odd parity modes, integration of Eq. (B15), combined with the asymptotic form of h_0^{RW} and h_1^{RW}, yields $\kappa = -1/(2M)\int dt'\,\psi_{RW}(t')$.

From these, and Eqs. (B8) and (B9), we obtain G^{IRG} and h_2^{IRG}, which are used to reconstruct the gravitational perturbation tensor:

$$h_{AB}^{IRG} = 2M\left[\psi_{ZM}V_{AB}^{lm} + 2\int dt'\,\psi_{RW}(t')W_{AB}^{lm}\right] + \mathcal{O}(f). \tag{B18}$$

Again, the Zerilli-Moncrief and Regge-Wheeler functions have l and m multipole indices, and there is an implicit summation over them. The components h_{AB}^{IRG} [without the $\mathcal{O}(f)$ correction] contains all the information about the energy and angular momentum absorbed by the black hole. It is then meaningful to refer to these components as the radiative part of the perturbation tensor in the vicinity of the event horizon. In analogy with the far zone definitions, the two gravitational-wave polarizations are defined as $h_+ = h_{\theta\theta}^{IRG}/4M^2$ and $h_\times = h_{\theta\varphi}^{IRG}/(4M^2\sin\theta)$. They are given in Eq. (3.2).

3. Radiation zone fluxes

In terms of its tetrad components, the perturbation tensor in the outgoing radiation gauge is

$$\begin{aligned}
h_{\mu\nu}^{ORG} = {} & h_{ll}n_\mu n_\nu + 2(h_{l\bar{m}}n_{(\mu}m_{\nu)} + h_{lm}n_{(\mu}\bar{m}_{\nu)})\\
& + h_{\bar{m}\bar{m}}m_\mu m_\nu + h_{mm}\bar{m}_\mu\bar{m}_\nu,
\end{aligned} \tag{B19}$$

where $h_{vv}=h_{\mu\nu}v^\mu v^\nu$, for any vector v^μ belonging to the tetrad. To leading order in r^{-1}, the tetrad components are

$$h_{ll}\sim\mathcal{O}(r^{-2}),$$

$$h_{lm}\sim\mathcal{O}(r^{-2}),$$

$$h_{\bar{m}\bar{m}}=\frac{1}{r^2}h^{ORG}_{AB}\bar{m}^A\bar{m}^B,$$

$$h_{mm}=\frac{1}{r^2}h^{ORG}_{AB}m^Am^B, \tag{B20}$$

where the vector $m^A=r(\partial\theta^A/\partial x^\mu)m^\mu$, and h^{ORG}_{AB} is given in Eq. (B13).

Calculating the covariant derivative of $h^{ORG}_{\mu\nu}$ and substituting the result in Eq. (B1), we get

$$T_{\mu\nu}=\frac{1}{64\pi}[\,\eta^{\alpha\beta}{}_\mu\eta^*_{\alpha\beta\nu}+\eta^{\alpha\beta}{}_\mu\rho^*_{\alpha\beta\nu}+\rho^{\alpha\beta}{}_\mu\eta^*_{\alpha\beta\nu}+\rho^{\alpha\beta}{}_\mu\rho^*_{\alpha\beta\nu}]+\text{c.c.}, \tag{B21}$$

where

$$\eta_{\alpha\beta\mu}=h_{ll,\mu}n_\alpha n_\beta+2h_{lm,\mu}n_{(\alpha}\bar{m}_{\beta)}+2h_{l\bar{m},\mu}n_{(\alpha}m_{\beta)}+h_{mm,\mu}\bar{m}_\alpha\bar{m}_\beta+h_{\bar{m}\bar{m},\mu}m_\alpha m_\beta,$$

$$\rho_{\alpha\beta\mu}=h_{ll}[n_\alpha n_\beta]_{;\mu}+2h_{lm}[n_{(\alpha}\bar{m}_{\beta)}]_{;\mu}+2h_{l\bar{m}}[n_{(\alpha}m_{\beta)}]_{;\mu}+h_{mm}[\bar{m}_\alpha\bar{m}_\beta]_{;\mu}+h_{\bar{m}\bar{m}}[m_\alpha m_\beta]_{;\mu}. \tag{B22}$$

The first term appearing in Eq. (B21) can be calculated exactly. It is

$$\eta^{\alpha\beta}{}_\mu\eta^*_{\alpha\beta\nu}=h_{mm,\mu}h^*_{\bar{m}\bar{m},\nu}+h_{\bar{m}\bar{m},\mu}h^*_{mm,\nu}. \tag{B23}$$

Evaluating the remaining terms requires more effort. They involve products of tetrad vectors and their covariant derivatives. It is easy to show that the only non-vanishing t, r, and φ components are $m^\alpha n_{\alpha;\varphi}=-(\sqrt{2}/4)\imath f\sin\theta$, $\bar{m}^\alpha m_{\alpha;\varphi}=-\imath\cos\theta$, and $m^\alpha_{;\varphi}n_{\alpha;r}=\sqrt{2}M/(4r^2)\imath\sin\theta$. Using these and Eq. (B20), we find that

$$T_{tr}=-\frac{1}{32\pi}(\dot{h}_{mm}\dot{h}^*_{\bar{m}\bar{m}}+\dot{h}_{\bar{m}\bar{m}}\dot{h}^*_{mm}), \tag{B24}$$

$$T_{r\varphi}=-\frac{1}{64\pi}(\dot{h}_{mm}h^*_{\bar{m}\bar{m},\varphi}+\dot{h}_{\bar{m}\bar{m}}h^*_{mm,\varphi})+\frac{\imath}{64\pi}(\dot{h}_{mm}h^*_{\bar{m}\bar{m}}+\dot{h}_{\bar{m}\bar{m}}h^*_{mm})\cos\theta+\text{c.c.}, \tag{B25}$$

where we replaced r derivatives with t derivatives, and neglected terms of order $\mathcal{O}(r^{-3})$ and higher.

These expressions for the stress-energy tensor can be used to calculate the fluxes in the radiation zone. Inserting Eq. (B24) into the first of Eq. (B4), where we set $\epsilon=1$ and $f\approx1$, yields

$$\frac{dE}{dt}=\frac{r^2}{32\pi}\int d\Omega(\dot{h}_{mm}\dot{h}^*_{\bar{m}\bar{m}}+\dot{h}_{\bar{m}\bar{m}}\dot{h}^*_{mm})=\frac{1}{32\pi}\int d\Omega\dot{h}_{AB}\dot{h}^{*AB}$$

$$=\frac{1}{32\pi}\sum_{lm}\sum_{l'm'}\int d\Omega[\,|\dot{\psi}_{ZM}|^2V^{lm}_{AB}V^{*AB}_{l'm'}+4|\psi_{RW}|^2W^{lm}_{AB}W^{*AB}_{l'm'}]$$

$$=\frac{1}{64\pi}\sum_{lm}\frac{(l+2)!}{(l-2)!}[\,|\dot{\psi}_{ZM}|^2+4|\psi_{RW}|^2], \tag{B26}$$

where in the first equality we use $\Omega^{AC}\Omega^{BD}h_{AB}h^*_{CD}=r^2(h_{mm}h^*_{\bar{m}\bar{m}}+h_{\bar{m}\bar{m}}h^*_{mm})$, the second equality follows from Eq. (B13), and the third equality follows from evaluating the angular integral with the aid of

$$\int d\Omega V^{lm}_{AB}V^{AB*}_{l'm'}=\frac{1}{2}\frac{(l+2)!}{(l-2)!}\delta_{ll'}\delta_{mm'},$$

$$\int d\Omega W^{lm}_{AB}W^{AB*}_{l'm'}=\frac{1}{2}\frac{(l+2)!}{(l-2)!}\delta_{ll'}\delta_{mm'}.$$

The angular momentum flux calculation follows similar steps. Inserting Eq. (B25) into the second of Eq. (B4), we get

$$\frac{dL}{dt}=-\frac{r^2}{64\pi}\int d\Omega[(\dot{h}_{mm}h^*_{\bar{m}\bar{m},\varphi}+\dot{h}_{\bar{m}\bar{m}}h^*_{mm,\varphi})-\imath(\dot{h}_{mm}h^*_{\bar{m}\bar{m}}+\dot{h}_{\bar{m}\bar{m}}h^*_{mm})\cos\theta]+\text{c.c.} \tag{B27}$$

The last term involves the product of $\cos\theta$ with a term of the form $\sin\theta S^{lm}(\theta)S^*_{l'm'}(\theta)$, where $S^{lm}(\theta)$ is a spherical harmonic function. Under the interchange $\theta\to\pi-\theta$, we have that $\cos\theta\to-\cos\theta$ and $\sin\theta S^{lm}(\theta)S^*_{l'm'}(\theta)\to\sin\theta S^{lm}(\theta)S^*_{l'm'}(\theta)$. The overall term is therefore odd in θ with respect to $\pi/2$, and integration over $0\leqslant\theta\leqslant\pi$ yields zero contribution to the angular momentum flux. We are then left with

$$\frac{dL}{dt} = -\frac{r^2}{64\pi}\int d\Omega(\dot{h}_{mm}h^*_{\overline{mm},\varphi} + \dot{h}_{\overline{mm}}h^*_{mm,\varphi} + \text{c.c.})$$

$$= \frac{\imath m r^2}{64\pi}\int d\Omega(\dot{h}_{mm}h^*_{\overline{mm}} + \dot{h}_{\overline{mm}}h^*_{mm} + \text{c.c.})$$

$$= \frac{\imath m}{64\pi}\int d\Omega(\dot{h}^{AB}h^*_{AB} + \text{c.c.})$$

$$= \sum_{lm}\sum_{l'm'}\frac{\imath m}{64\pi}\int d\Omega\Bigg[\dot{\psi}_{ZM}\psi^*_{ZM}V^{lm}_{AB}V^{*AB}_{l'm'} + 4\psi_{RW}\int_{-\infty}^{t} dt'\,\psi^*_{RW}(t')W^{AB}_{lm}W^{*AB}_{l'm'}\Bigg] + \text{c.c.}$$

$$= \sum_{lm}\frac{\imath m}{128\pi}\frac{(l+2)!}{(l-2)!}\Bigg[\dot{\psi}_{ZM}\psi^*_{ZM} + 4\psi_{RW}\int_{-\infty}^{t} dt'\,\psi^*_{RW}(t')\Bigg] + \text{c.c.}, \tag{B28}$$

where we use $h_{\overline{mm},\varphi} = -\imath m h_{\overline{mm}}$ in the first equality, and the remaining steps shadow the ones for the energy flux calculation.

4. Black hole absorption

The calculation of the black hole absorption is similar to the calculation of the far-zone fluxes. Here we are looking to isolate the divergent piece of $T_{\mu\nu}$, since it is this part that corresponds to the blueshifted gravitational waves: The expansion parameter is f, and we are looking for the $\mathcal{O}(f^{-1})$ portion of the tr and $r\varphi$ components of $T_{\mu\nu}$. We neglect terms of order $\mathcal{O}(1)$.

The material developed in Sec. B 3 can be used here simply by replacing $l^\mu \leftrightarrow n^\mu$. In an ingoing radiation gauge, the non-trivial tetrad components of the perturbation tensor are

$$h_{nn} \sim \mathcal{O}(f),$$

$$h_{nm} \sim \mathcal{O}(f),$$

$$h_{\overline{mm}} = \frac{1}{4M^2}h^{IRG}_{AB}\overline{m}^A\overline{m}^B,$$

$$h_{mm} = \frac{1}{4M^2}h^{IRG}_{AB}m^A m^B, \tag{B29}$$

and m^A was introduced previously.

With the replacement $n^\nu \leftrightarrow l^\nu$, the steps we follow are almost exactly the same as those of the radiation zone calculations. The stress-energy tensor is written as in Eq. (B21), with $\eta_{\alpha\beta\mu}$ and $\rho_{\alpha\beta\nu}$ changed to reflect the exchange of tetrad vectors. It is not difficult to show that the non-vanishing components of the contracted derivatives of the tetrad vectors are now $m^\alpha l_{\alpha;\varphi} = (\sqrt{2}/2)\imath \sin\theta$, $\overline{m}^\alpha m_{\alpha;\varphi} = -\imath\cos\theta$, and $m^\alpha{}_{;\varphi} l_{\alpha;r} = \sqrt{2}M/(2r^2)\imath f^{-1}\sin\theta$.

These, combined with Eq. (B29), reveal that the relevant components of the stress-energy tensor are given by

$$T_{tr} = -\frac{f^{-1}}{32\pi}(\dot{h}_{mm}\dot{h}^*_{\overline{mm}} + \dot{h}_{\overline{mm}}\dot{h}^*_{mm}), \tag{B30}$$

$$T_{r\varphi} = -\frac{f^{-1}}{64\pi}(\dot{h}_{mm}h^*_{\overline{mm},\varphi} + \dot{h}_{\overline{mm}}h^*_{mm,\varphi}) + \frac{\imath f^{-1}}{64\pi}(\dot{h}_{mm}h^*_{\overline{mm}} + \dot{h}_{\overline{mm}}h^*_{mm})\cos\theta + \text{c.c.}, \tag{B31}$$

where we replaced r^* derivatives with t derivatives and neglected term of order $\mathcal{O}(1)$. Note that this is exactly of the same form (apart from a factor of f^{-1}) as that obtained for T_{tr} and $T_{r\varphi}$ in the far zone.

To calculate the fluxes, we insert these expressions into Eq. (B4), where we also set $\epsilon = -1$. The divergence in the stress-energy tensor is canceled by the factor of f appearing in Eq. (B4). The remaining calculations are identical with those of the far zone, with h^{IRG}_{AB} given by Eq. (B18). The energy flux is

$$\frac{dE}{dt} = \sum_{lm}\frac{1}{64\pi}\frac{(l+2)!}{(l-2)!}[|\dot{\psi}_{ZM}|^2 + 4|\psi_{RW}|^2], \tag{B32}$$

while the angular momentum flux is

$$\frac{dL}{dt} = \sum_{lm}\frac{\imath m}{128\pi}\frac{(l+2)!}{(l-2)!}\Bigg[\dot{\psi}_{ZM}\psi^*_{ZM} + 4\psi_{RW}\int_{-\infty}^{t} dt'\,\psi^*_{RW}(t')\Bigg] + \text{c.c.} \tag{B33}$$

[1] K. Danzmann *et al.*, "LISA—Proposal for a Laser-Interferometric Gravitational Wave Detector in Space," Max-Planck-Institut für Quantenoptic Report No. MPQ 177, 1993; K. Danzmann *et al.*, "LISA—Laser Interferometer Space Antenna, Pre-Phase A Report," Max-Planck-Institut für Quantenoptic Report No. MPQ 233, 1998.

[2] J. Kormendy and D. Richstone, Annu. Rev. Astron. Astrophys. **33**, 581 (1995).

[3] J. Miralda-Escudé and A. Gould, astro-ph/0003269.

[4] S. Sigurdsson and M.J. Rees, Mon. Not. R. Astron. Soc. **284**, 847 (2000).

[5] S. Sigurdsson, Class. Quantum Grav. **14**, 1425 (1997).

[6] F.J. Zerilli, Phys. Rev. D **2**, 2141 (1970); Phys. Rev. Lett. **24**, 737 (1970).

[7] V. Moncrief, Ann. Phys. (N.Y.) **88**, 323 (1974).

[8] T. Regge and J.A. Wheeler, Phys. Rev. **108**, 1063 (1957).

[9] C.O. Lousto and R.H. Price, Phys. Rev. D **56**, 6439 (1997).

[10] K. Martel and E. Poisson, Phys. Rev. D **66**, 084001 (2002).

[11] K. Glampedakis and D. Kennefick, Phys. Rev. D **66**, 044002 (2002); K. Glampedakis, S.A. Hughes, and D. Kennefick, *ibid.*

66, 064005 (2002).
[12] C. Cutler, D. Kennefick, and E. Poisson, Phys. Rev. D **50**, 3816 (1994).
[13] S.A. Teukolsky, Astrophys. J. **185**, 635 (1973).
[14] R. Lopez-Aleman, G. Khanna, and J. Pullin, Class. Quantum Grav. **20**, 3259 (2003).
[15] W.H. Press, S.A. Teukolsky, and W.T. Vetterling, *Numerical Recipes in C* (Cambridge University Press, New York, 1997).
[16] J.N. Goldberg, A.J. MacFarlane, E.T. Newman, F. Rohrlich, and E.C.G. Sudarshan, J. Math. Phys. **8**, 1768 (1991).
[17] R.A. Isaacson, Phys. Rev. **166**, 1272 (1968).
[18] P.C. Peters, Phys. Rev. B **136**, B224 (1964).
[19] E. Poisson, Phys. Rev. D **47**, 1497 (1993).
[20] E. Poisson, Phys. Rev. D **52**, 5719 (1995); **55**, 7980 (1997).
[21] E. Poisson and M. Sasaki, Phys. Rev. D **51**, 5753 (1995).
[22] K. Alvi, Phys. Rev. D **64**, 104020 (2001).
[23] P.L. Chrzanowski, Phys. Rev. D **11**, 2042 (1975).